Ocean Engineering, Volume 312, November 2024, Article number 119312
DOI:10.1016/j.oceaneng.2024.119312

A Study into the Correlation between Single Array-Hull Configurations and Wave Spectrum for Floating Solar Photovoltaic Systems

Mohammad Izzuddin Jifaturrohman[1], I Ketut Aria Pria Utama[2*], Teguh Putranto[2], Dony Setyawan[2], Luofeng Huang[3].

[1] Department of Ocean Engineering, Faculty of Marine Technology, Institut Teknologi Sepuluh Nopember, Indonesia

[2] Department of Naval Architect, Faculty of Marine Technology, Institut Teknologi Sepuluh Nopember, Indonesia

[3] Faculty of Engineering and Applied Sciences, Cranfield University, Cranfield, MK 43 0AL, UK

Corresponding author: *kutama@its.ac.id (I Ketut Aria Pria Utama)

Abstract

Floating photovoltaic (FPV) systems offer a viable renewable energy solution due to easy installation and cost-effectiveness compared to other renewable energy generation methods. On the other hand, land-based solar photovoltaics face challenges such as space scarcity and environmental impacts. Shifting to nearshore locations unlocks vast ocean space potential, though waves expose significant challenges to FPV systems. Several novel FPV system designs are proposed, inspired by high-speed vessel multihulls, including catamaran, trimaran, quadrimaran, and pentamaran configurations, as floating supports for solar panels. Simulations were conducted to determine Response Amplitude Operators (RAOs) under various irregular wave spectrum conditions in a free-floating initial state. The FPV motion problem was solved using linear potential-flow theory with the Boundary Element Method (BEM) with Green-Function approach. Superposition of wave spectral energy and motion RAOs was used to obtain spectral structural responses. Motion in heave, roll, and pitch modes was evaluated across wave spectrum types. Results show that adding hulls reduces the significant amplitude response in all motion modes. In summary, valuable insights into floater designs and the hydrodynamic evaluation of FPV systems are presented.

Keywords: BEM, Floating photovoltaic; Multihull structures; Nearshore technology; Seakeeping performance; Wave spectrums.

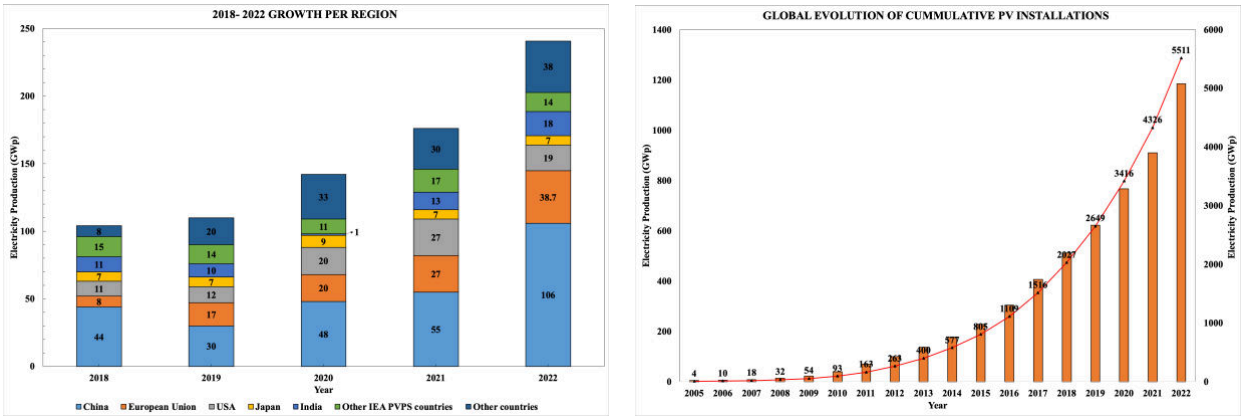
1. Introduction

1.1. Background

The global evolution of photovoltaic technology indicates a growing optimistic outlook. According to the IEA (2023) from 2018 to 2022, a rapid increase in the photovoltaic (PV) technology market has been observed,

Published by Elsevier. This is the Author Accepted Manuscript issued with: Creative Commons Attribution License (CC:BY 4.0).
The final published version (version of record) is available online at DOI:10.1016/j.oceaneng.2024.119312. Please refer to any applicable publisher terms of use.

with China leading as the top global market, followed by other countries (**Figure 1a**). By the end of 2022, the global minimum total installed capacity is projected to reach 1185 GWp, as depicted in **Figure 1b.**



(a) (b)

Figure 1. Annual (a) & cumulative (b) photovoltaic (PV) installations throughout time, redrawn from (IEA, 2023).

By 2022, global emissions of carbon dioxide (CO2) gas from energy combustion and industrial processes grew by 0.9% or about 321 metric tons (abbreviated as Mt hereinafter) to an all-time high of 36800 Mt (IEA, 2022). This underscores the critical urgency for advancing renewable energy technologies, particularly PV systems. PV technology, which saved approximately 1399 Mt of CO2 emissions annually in 2022, plays a pivotal role in mitigating these emissions and reducing the carbon footprint associated with electricity generation (Bošnjaković et al., 2023).

Although PV cells have improved in efficiency, they still generate less electric power per unit area compared to geothermal power plants (Xie et al., 2022; Yan et al., 2022). The issue of land availability presents a substantial obstacle to the establishment of PV power plants, especially in countries with limited land capacity (Vyas et al., 2022). For instance, setting up a 1 MWp power plant requires approximately 10000 square meters (abbreviated as m^2 hereinafter) of land area, assuming a solar panel efficiency of 15%. While the efficiency of PV modules has improved to 20%, the fundamental challenge of land use and the environmental impact associated with their deployment remains unchanged (Ghosh, 2023). Furthermore, a study by Pimentel Da Silva and Branco (2018) highlighted environmental concerns related to PV installations, including deforestation, habitat loss leading to bird extinction, erosion, runoff, and microclimate changes. These factors emphasize the complex considerations involved in land-based PV technology deployment.

The importance of redesigning land-based PV installations towards spatial strategies that provide greater flexibility, such as deploying photovoltaic systems over water bodies—a concept known as Floating Photovoltaics (FPV)—is emphasized. FPV systems are increasingly preferred in urban areas due to their ability to mitigate high land costs. The presence of natural water bodies enhances the efficiency of photovoltaic systems by providing additional cooling and encountering fewer shading obstacles. Moreover, reduced dust accumulation is experienced by FPV systems compared to ground-based PV systems.

The efficiency of FPV technology can be significantly improved when deployed in near-shore areas, as ocean spaces offer a much larger technical area compared to the limited surface area of water dams. Additionally, according to a study by Wang et al. (2019), nearly 50% of the world's population lives within 100000 meters (abbreviated as m hereinafter) of the ocean coastline, making the installation of FPVs a viable solution to meet their energy demands.

Nevertheless, understanding the challenging conditions in which FPV systems interact in the ocean is crucial. Liu et al. (2018) identified various external variables that impact FPV systems, including wind, waves, currents, biofouling, and long-term UV deterioration. Hence, proper design is necessary for FPV systems to withstand strong winds and hydrodynamic forces generated by the interaction between waves and currents. Wave-induced motion can alter the tilt angle of solar panels, impacting energy production. Additionally, significant wave loads could jeopardize the structural integrity of FPV systems . (Delacroix et al., 2023; Wei et al., 2023; Zhang et al., 2024). High salinity concentrations can also lead to corrosion, potentially reducing the lifespan of the support structure. Therefore**, Figure 2** will illustrate the key considerations in coherence with the pros and cons of using FPV technology.

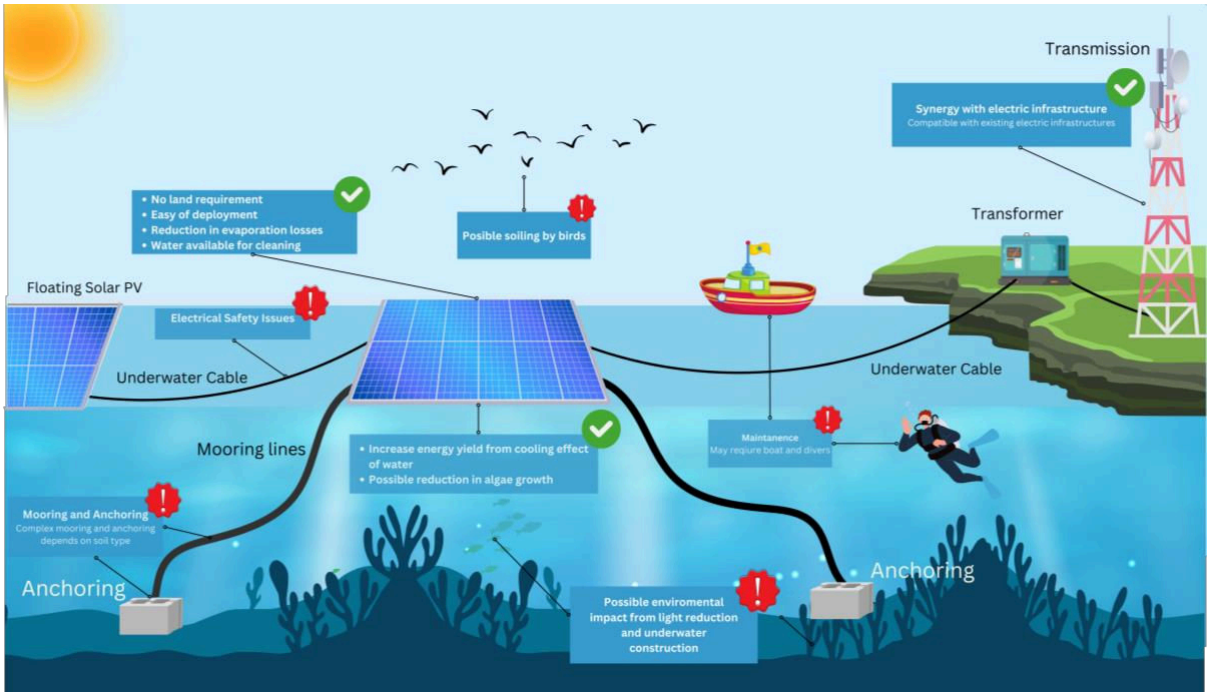


Figure 2. An illustration demonstrating the primary benefits and possible drawbacks of FPV systems, redrawn from (Pouran et al., 2022)

1.2. A Review of Numerical Models Applied to Floating Photovoltaic Systems in Offshore Environments

This section provides a summary of notable contributions in numerical computing with the CFD approach that has advanced in this field. In the study conducted by Trapani & Millar (2016), the motion and stress on a flexible thin-film PV system caused by regular waves were analyzed using CFD techniques. Xu & Wellens (2022a) evaluated the nonlinear interaction between waves and offshore FPV systems, focusing on the hydro-elastic wave model and deriving related analytical solutions. Xu & Wellens (2022b) further developed their investigation by conducting third-order analytical solutions, showcasing the engineering practicality of their technique for designing FPV structures in different water depths.

Several investigation studies by Hu et al. (2013) and Friel et al. (2020) examined the impact of environmental and platform characteristics on the hydrodynamic performance of FPVs. The numerical findings were validated using model experiments. It was found by Zheng et al. (2020) that the hydrodynamic performance of FPV platforms utilizing innovative semi-submersible designs is generally favourable. This indicates that such designs can effectively manage hydrodynamic forces, enhancing the stability and performance of floating photovoltaic systems.

As FPV projects progress, their installed capacity increases, resulting in larger platforms that are more exposed to significant wave loads. To tackle these difficulties, modular floating platforms are presently the focus of efforts described by Essak & Ghosh (2022) and Wang & Lund (2022). Modularization offers an economically efficient option for the entire process, including manufacturing, transportation, and installation. These modular solutions offer both scalability and simplified installation and maintenance for localized components - in the event of a minor issue, it is possible to fix this without dismantling the entire FPV system. Moreover, as indicated by Cazzaniga et al. (2018), this idea can mitigate hydroelastic structural problems compared to integrated single-structure solutions.

Additionally, the safety and reliability of components in large-scale floating solar power plants are emphasized by Choi & Lee (2015). Thus, the examination by Cao et al. (2021) and Li et al. (2023) focuses on the appearance of nonlinearities due to hydrodynamic effects from multiple objects and their internal interactions in ocean waves and modular solar systems. New design solutions to address challenges posed by extreme environmental conditions are consistently being developed by multiple studies. The research conducted by Cazzaniga & Rosa-Clot (2021) and Michailides et al. (2013) investigates the design technique for Modularized Floating Solar (MFS) and has improved its design to enhance performance and efficiency, considering various module layouts (grid types) and mechanical properties based on performance criteria. This technique involves the utilization of FPV modules with identical specifications and joint connectors to develop a multi-body FPV platform system. A significant focus of the study on MFS has been on the design of the joint connector, a crucial structural element that affects sensitivity to dynamic motions. Consequently, studies by Zhang et al. (2022, 2023) have been conducted on the single-array arrangement, examining both free-floating structures and those with hinged connections. CFD methodologies and model testing in a towing tank at Inha University for the MFS FPV model were utilized in a study by Lee et al. (2022). The study focused on analyzing the dynamic response of a multi-body FPV platform under different sea conditions with complex motion characteristics when subjected to hinged connector boundary conditions (BC).

The advanced study by Wei et al. (2024) focused on bridging a research gap in the field of MFS. Specifically, MFS configurations of different sizes, such as 7×7, 9×7, 11×7, and 13×7, were examined, highlighting the challenges of simulating complicated interactions between individual floating bodies using multibody dynamics principles. An innovative parameterization was introduced in their study, which considers the correlation between the ratio of structural length to wavelength and the motion of floating objects. This alternative method has fascinating implications for predicting and reporting the motion characteristics of solar

122 farms in wave conditions. Unfortunately, a lack of research on the hydrodynamic efficiency of multi-body FPV
123 platforms was discovered by Song et al. (2022). This observation is supported by a limited number of well-
124 documented successful installation efforts in this scope. Yan et al. (2023) have identified that the obstacle arises
125 from a limited understanding of the hydrodynamic effects experienced by multi-body marine FPVs in challenging
126 situations. Their limited comprehension has hindered commercial development in addressing ocean spatial
127 requirements. Therefore, design structural analysis recommendations are crucial to ensuring the safety and
128 efficient operation of these connectors in MFS systems.
129

130 **1.3. A Review of Numerical Technique Solver Approaches for Seakeeping**

131 In naval architecture and ocean engineering, accurate seakeeping analysis—predicting ship motions and
132 wave loads—is essential for optimizing marine structures. As stated by Li & Li (2019), computational methods
133 for this analysis are typically categorized into potential flow theory-based approaches and Reynolds-Averaged
134 Navier-Stokes (RANS) methods. Among potential flow methods, Green's function techniques are widely used
135 for solving boundary value problems around a ship's hull, particularly for free-surface interactions. These
136 techniques are effective in capturing the dynamic interactions between the ship and surrounding fluid, especially
137 in environments with wavy-free surfaces (Newman, 1979). The Boundary Element Method (BEM) combined
138 with the free-surface Green function has received considerable attention in recent research. X. Chen & Liang
139 (2016) demonstrated that this combination simplifies the boundary integral equation to an integral over the ship's
140 body surface (including the waterline if required), thus reducing computational complexity and the number of
141 unknowns. Additionally, Sclavounos & Nakos (1990) showed that using the free-surface Green function reduces
142 dispersion errors associated with free-surface discretization. The free-surface Green function, representing a unit-
143 strength source potential, inherently satisfies both free-surface and far-field radiation conditions (Wehausen &
144 Laitone, 1960). Applied within a BEM framework, it provides a comprehensive solution that accurately meets all
145 relevant boundary conditions, making it a crucial tool in advanced seakeeping analysis.

146 Another widely used method for seakeeping analysis is the Rankine panel method, which is favored for its
147 flexibility in managing complex free-surface conditions. However, based on He & Kashiwagi (2014), it requires
148 discretizing the free surface around the body, which increases the number of unknowns and can lead to numerical
149 dispersion, dissipation, and instability. In time-domain 3D seakeeping methods, the Rankine panel method often
150 offers advantages over the free-surface Green-function method (He, 2014), especially for ships with forward
151 speed, due to its simpler application despite the need for a damping zone and extensive free surface discretization

(Ten & Chen, 2010). Higher Order Boundary Element Methods (HOBEM) have become popular due to their efficiency in handling complex geometries and multibodies. Unlike traditional constant panel methods, HOBEM uses higher-order elements to discretize boundary surfaces, reducing the stepwise discretization problems. This results in a smoother representation of the velocity potential and its derivatives, requiring fewer elements and simplifying the evaluation of spatial flow derivatives. Additionally, ITTC (2012) stated that HOBEM has maintained computational efficiency without complicating the code. HOBEM has been effectively used to assess wave loads and body motions at both zero speed (He, 2014) and forward speeds (Kashiwagi & He, 2014). Shao & Faltinsen (2014) introduced a time-domain HOBEM utilizing cubic shape functions to tackle second-order problems related to wave steepness and tangship motions. This method, formulated in a body-fixed coordinate system, addresses numerical challenges associated with higher-order derivatives and was applied to study second-order wave excitation and ship springing for a modified Wigley hull in monochromatic and bichromatic waves.

In the Rankine-Green matching method, the flow field is divided into two regions: an inner domain and an outer domain. The Rankine function is employed in the inner domain, as described by Tang et al. (2021), while the free-surface Green function is applied in the outer domain. An artificial control surface, represented by a simple regular wall, is utilized to prevent numerical divergence of the Green function at the free surface, as noted by (Tang et al., 2020). This method leverages the advantages of both functions. Specifically, the Rankine source is utilized within the inner domain, which includes the ship's hull and part of the free surface, applying the boundary element method to address free-surface conditions. In the outer domain, extending from the control surface to infinity, the Green function is used to satisfy linear boundary conditions on the free surface. The control surface is modeled as a vertical cylindrical surface, where the velocity potential and its radial derivative are expanded using Laguerre and Fourier series. This setup allows the boundary integral equation to relate the velocity potential to its radial derivative, as demonstrated by (Liang & Chen, 2017).

Lagemann (2019) examined computational fluid dynamics (CFD) methods, which solve the Navier-Stokes equations and are referred to as "computational flow methods." Unlike potential flow methods, CFD methods incorporate viscous effects, necessitating significantly more computational resources. These methods include Reynolds-Averaged Navier-Stokes (RANS), which averages turbulent fluctuations over time, as well as Large-Eddy Simulations (LES) and Direct-Eddy Simulations (DES), offering detailed turbulence resolution (Bertram, 2012). Despite ongoing advancements in LES, the RANS method remains the primary approach for industrial seakeeping simulations. Additionally, inviscid flow modeling using Euler-type equations provides an alternative approach. Complex flow phenomena such as separation and viscous effects cannot be adequately modeled using

potential flow theory alone. With advancements in computer science and technology, CFD methods utilizing RANS equations have become increasingly mature and popular, offering significant potential for enhancing ship design and evaluation. These methods effectively address strongly nonlinear issues arising from high forward speeds, large amplitude motions, and intense free surface interactions (Jiao et al., 2021).

2. Highlighting the Scope and Novel Aspects of the Paper

An innovative design for FPV platforms, specifically for ocean environments, has been introduced by integrating the multihull concept from naval engineering design principles related to high-speed vessels. Various floating structure designs have been proposed, ranging from catamarans (two hulls), trimarans (three hulls), and quadrimarans (four hulls) to pentamarans (five hulls), arranged laterally to provide floating space for solar installations. This geometric design aims to provide a relatively large deck space while utilizing hull configurations and dampers to enhance stability. The primary motivation for selecting this design is the potential shift towards nearshore locations, where marine loads are directly exposed. The floating structure must be strengthened and improved to withstand the harsh hydrodynamic conditions of waves, currents, and wind, which represent a significant difference from the existing common models used in the relatively calm waters of lakes.

The initial assessment involves analyzing a free-floating state to determine the impact of natural oscillation motion caused by wave propagation in regular waves within the frequency domain.

Additionally, this paper focused on analyzing the significant amplitude response motion (ζ_S) of single-array FPV systems as well as accommodating sensitivity to various types and modifications of wave spectra, including Pierson-Moskowitz (PM), JONSWAP $\gamma = 2$, JONSWAP $\gamma = 2.5$, JONSWAP $\gamma = 3.3$, ITTC - 1975, and ISSC - 1964. Hydrodynamic motions have been examined across sea states ranging from sea states 2 to 5, providing valuable insights into performance and correlations among all aspects considered.

Therefore, **Figure 3** presents a comprehensive scheme characterized by several variables: independent variables, dependent variables, and control variables. Each variable has significance for the results of the study. The independent variables account for various aspects of variation implemented in the study. The dependent variables represent the qualitative objective values for each aspect within the independent variables. Meanwhile, control variables are parameters that are maintained constant as equal components of comparison.

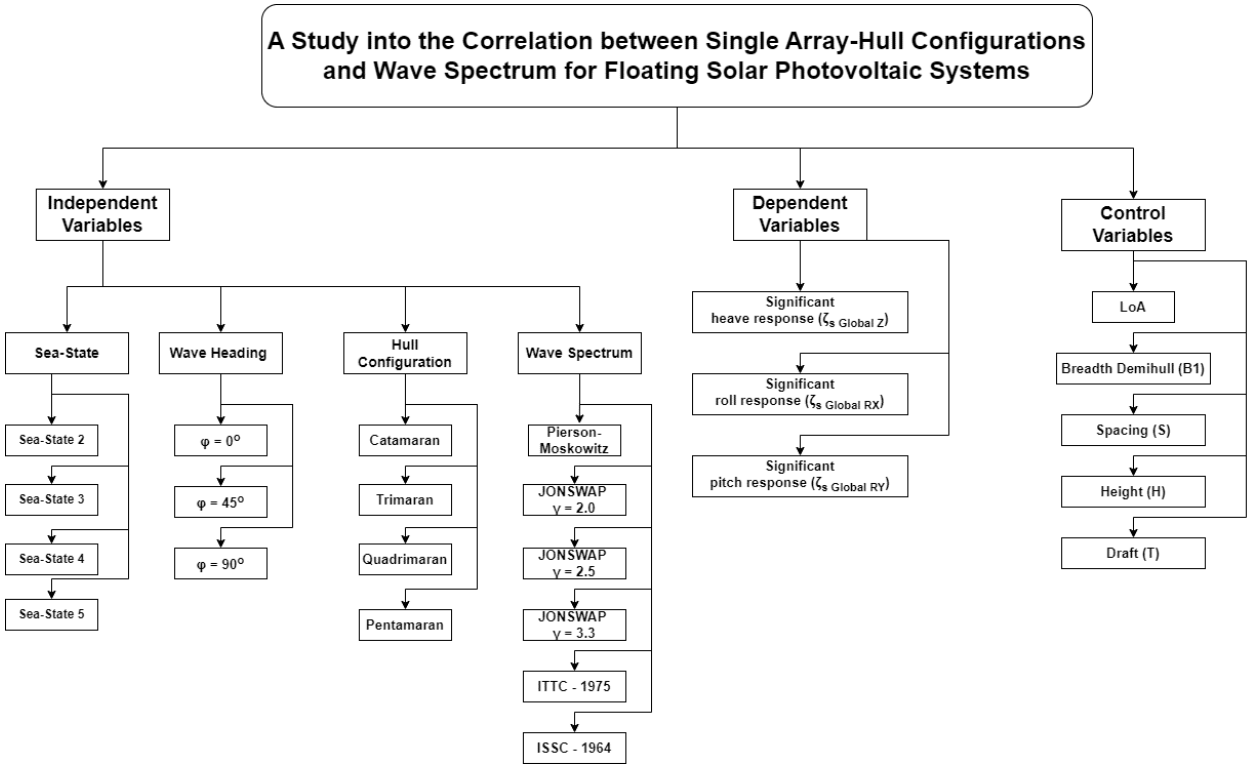


Figure 3. Scope of Research

3. The Limitations and Strengths of this Study

As outlined in **Section 2**, the novelty of this study lies in its approach to assessing seakeeping performance. An initial rapid assessment was conducted to evaluate the quality of the generated motions across various combinations of variables, as depicted in **Figure 3**. This preliminary evaluation serves as a critical step in determining the viability of the proposed method.

According to Bunnik et al. (2010), frequency-domain potential solvers provide the advantage of rapid computation, significantly reducing processing time. This efficiency makes them highly effective for obtaining an initial, accurate assessment of a system's response characteristics. It is important to recognize that the numerical method employed in this study – 3D panel Green Function with BEM method has certain limitations, particularly when compared to other techniques like CFD for viscous fluid simulations and time-domain approaches. These advanced CFD methods are more effective at capturing the dynamics of large waves, near-resonant frequencies, and significant viscous forces, though they may require substantial computational resources and time (Alves, 2016). **Tables 1** and **Table 2** provide an overview of the limitations and strengths associated with the chosen numerical method.

227 **Table 1.** Strengths of the present study

Strengths	Description
Speed and efficiency	Allows for quicker problem-solving compared to the time domain method, providing responses in a shorter time (Orcina Ltd, 2024)
Suitable in linear systems	As observed by Faltinsen (1990) and Newman (1977), this approach is particularly suitable for systems that can be accurately modelled as linear and stationary, where both the dynamic loading and the response exhibit a linear relationship by an underlying stochastic process (Orcina Ltd, 2024). Additionally, it is assumed that the statistical properties remain constant over time.
Simplicity for regular waves	The analysis is simplified for situations involving small amplitude ship motions or regular waves, especially when the ship is moving at zero or low speeds in wave excitation is assumed to be a simple harmonic motion (Ballard, 2002).

228

229 **Table 2.** Limitation of the present study

Limitation	Description
Non-linear interaction and steady state wave model limitations	This approach neglects the effects of wind and currents, which can lead to drift forces, as well as the nonlinear interactions between waves and currents. These factors can significantly influence the motion and stability of floating structures. Particularly in moored conditions, non-linear time-domain simulations are crucial for accurately capturing the force-deflection characteristics of the mooring lines (Lewandowski, 2008).
Limitations in time-dependent problems	Not suitable for time-dependent nonlinearity and transient problems, whereas the time domain methods are particularly effective for addressing time-dependent and nonlinear issues in floating systems. These include transient hydroelastic effects, nonlinear hydrostatic coefficients, nonlinear roll damping using semi-empirical methods, transient behaviours of steady forces, nonlinear cable forces, manoeuvring under unsteady motions, large amplitude motions, water on deck, and variations in forward speed. (Kara, 2022).

Limitation	Description
Limitations in realistic fluid applications	Potential flow models have inherent limitations in accurately representing real fluid dynamics, particularly in capturing effects like flow separation and boundary layers. To address these limitations, CFD solutions using Reynolds-Averaged Navier-Stokes (RANS) equations are preferred, as they account for viscous and turbulent interactions with wave-making (Wackers et al., 2011). While potential flow solvers are efficient for scenarios where viscous effects can be neglected, RANS-based methods are more suitable for comprehensive analysis where viscous effects are significant (Lagemann, 2019).

Although the BEM based on frequency domain analysis has certain limitations, it nonetheless provides valuable insights and has significant applications in naval engineering, particularly in the performance assessment of advanced marine vehicles, which are partially related to the scope of this study.

Seakeeping analysis is a crucial aspect of naval engineering, and the methodologies employed in this study offer substantial benefits. These include the calculation of wave-induced forces, motion responses in pure oscillatory motion, irregular wave spectrums, structural spectrum responses, and significant amplitude motion derived from the frequency domain by Root Mean Square (RMS) of stochastic calculations. By leveraging panel methods or using the BEM model, a robust framework for efficiently assessing these critical factors is provided (Xu et al., 2020).

While panel methods assume potential flow, which inherently limits their ability to model viscous effects like boundary layers and flow separation, they remain highly effective for early-stage design processes. In particular, potential flow solvers like AQWA have demonstrated both accuracy and computational efficiency, making them invaluable tools in the preliminary design phases of naval vessels. In conclusion, the methodologies and findings from this study offer valuable insights and practical tools that can be directly applied to the naval engineering community.

4. Methodology

The 3D panel diffraction solution, based on the Boundary Element Method (BEM), provides a robust numerical approach for solving linear partial differential equations formulated as integral equations. BEM is highly effective in addressing seakeeping problems across both frequency and time domains, incorporating both

first and second-order effects (Pasquale, 2016). By discretizing the hull surface into small panels, the 3D-panel method accurately captures the complex geometry of a vessel (Lagemann, 2019). The subsequent subsection contains data about each proposed design, including initial main dimensions, electrical output capacity, and weight distribution, followed by an isometric view of 3D modeling. Significant response spectra ($\zeta_{s\ [Z]}$, $\zeta_{s\ [RX]}$, $\zeta_{s\ [RY]}$) are used to evaluate seakeeping performance followed by stochastic calculation to determine the area under the spectrum curve within various sea state conditions.

4.1. Model Description & Material Properties

The structure of the FPV floater remains consistent across all proposed design configurations. Variations in design configurations arise from the number of hulls utilized as supporting structures, with the technique involving lateral duplication of these hulls. Subsequently, symbols for various parameters related to the primary dimensions of the FPV floater structure are presented in **Figure 4.**

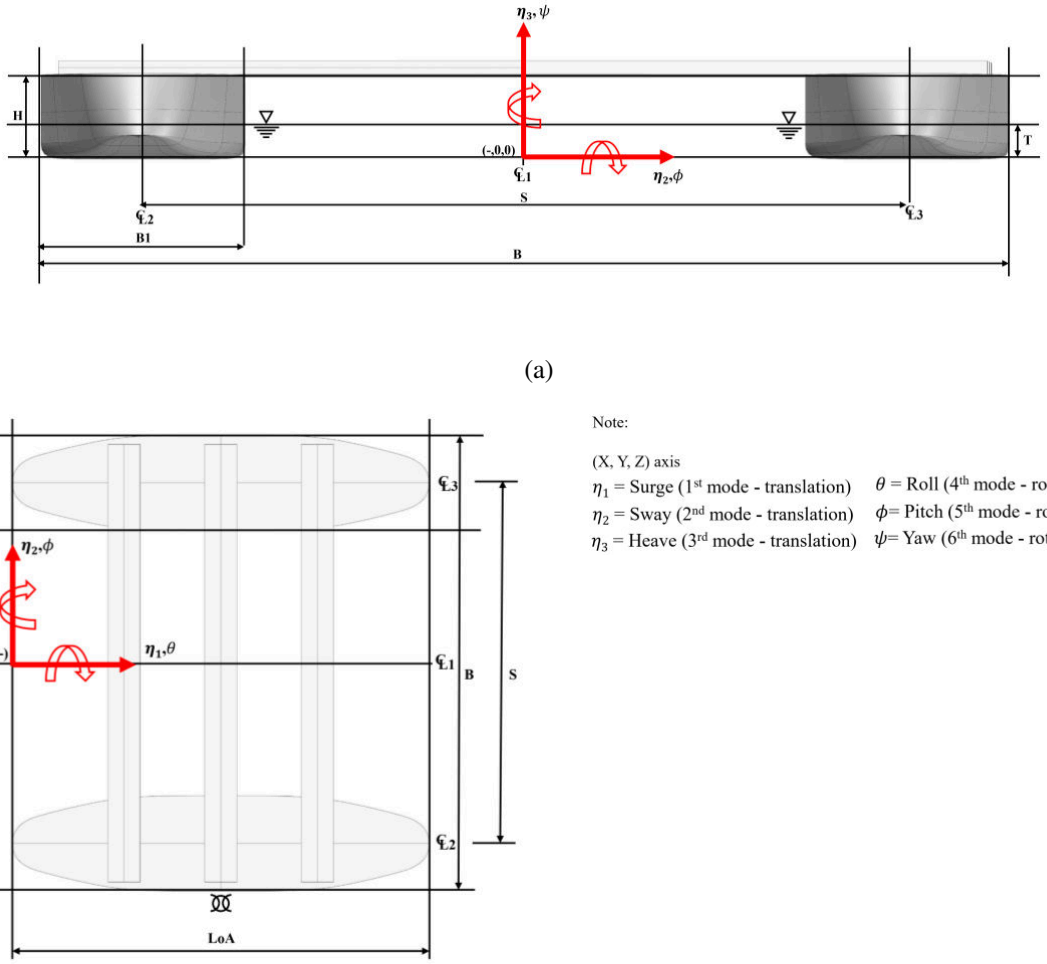


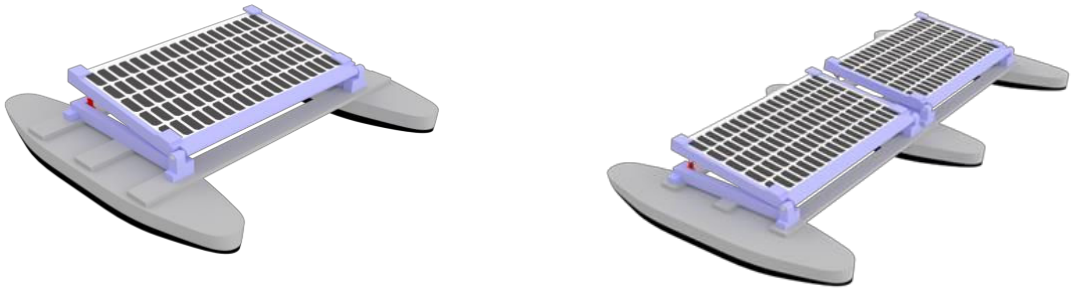
Figure 4. The sketch of the main dimension symbol in the FPV structure: (a) front view, (b) aerial view

The dimensions and hydrostatic parameters of each proposed floater design are listed in **Table 4**. Due to the similar geometry of the floater structures, most hydrostatic properties are identical, except for displacement. Additionally, the FPV structure design must be optimized to withstand harsh aquatic environmental conditions while maintaining lightweight material properties for economic feasibility. Therefore, High-Density Polyethylene (HDPE) material is employed, which facilitates easy implementation, reduces tension on the floating object due to hydrodynamic forces (Claus & López, 2022; Oliveira-Pinto & Stokkermans, 2020; World Bank Group, 2019), and is detailed in **Table 3**.

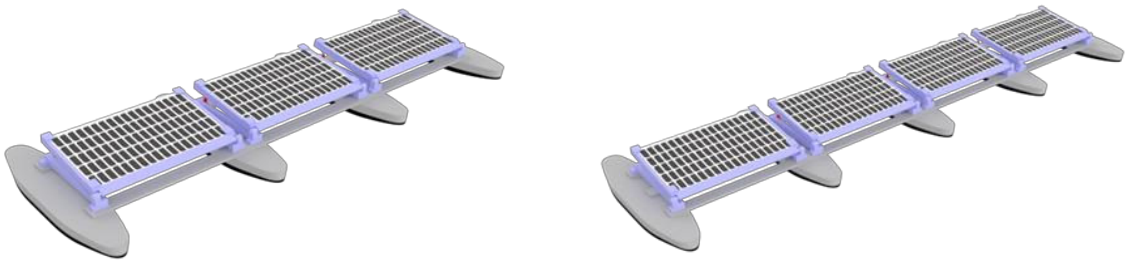
Table 3. Mechanical Properties of HDPE

Mechanical Properties	Value	Unit
Density	947	Kg/m^3
Tensile strength at yield	25	MPa
Elongation at yield	9	%
Modulus of elasticity in tension	1000	MPa
Modulus of elasticity in flexure	1000 - 1400	MPa

The 3D engineering design for various types of floaters in the FPV system is presented in isometric views in **Figure 5**. These designs, developed by Jifaturrohman et al. (2024) during the early phase of their research on nearshore energy generation, incorporated rigid connections using HDPE beams to support solar panels on each hull with identical main dimensions. The total installed power capacity for each proposed model, along with the specifications of the mono-crystalline technology utilized, is detailed in **Table 5**.



(a) (b)



(c) (d)

282

283 **Figure 5**. Isometric view of novel design in FPV: (a) catamaran, (b) trimaran, (c) quadrimaran, (d) pentamaran

284

285 **Table 4.** Main dimension and hydrostatic properties

Parameter	Catamaran	Trimaran	Quadrimaran	Pentamaran	Units
Lengthover All (LoA)	3.24	3.24	3.24	3.24	m
Breadth (B)	3.54	6.34	9.14	11.94	m
Height (H)	0.30	0.30	0.30	0.30	m
Draft (T)	0.12	0.12	0.12	0.12	m
Demihull Width (B1)	0.74	0.74	0.74	0.74	m
Spacing (S)	2.80	2.80	2.80	2.80	m
Hydrostatic values					
Displacement (Δ)	437.31	655.31	874.74	1094.17	kg
Block coefficient (Cb)	0.75	0.75	0.75	0.75	-
Prismatic coefficient (Cp)	0.76	0.76	0.76	0.76	-
Keel to buoyancy (KB)	0.06	0.06	0.06	0.06	m
Longitudinal Center of Buoyancy (LCB)	1.62	1.62	1.62	1.62	m

286

287 **Table 5.** Power output electrification energy

Parameter	Value	Unit	Remarks
PV capacity	665	Watt peak (Wp)	(CSI Solar Co. Ltd, 2021)
Module efficiency	21.40	%	

Parameter	Value	Unit	Remarks
Length of PV	2.38	m	
Width of PV	1.30	m	
PV module weight	34.40	kg	
Total installed capacity			
Catamaran	665	Watt peak (Wp)	These calculations are based
Trimaran	1330	Watt peak (Wp)	on the ideal capacity of the
Quadrimaran	1995	Watt peak (Wp)	considered mono-crystalline
Pentamaran	2660	Watt peak (Wp)	PV system.

4.2. Potential Flow Governing Equations

In seakeeping simulations, hydrodynamic forces (added masses, damping coefficients, wave forces) are computed using potential flow theory with Boundary Element Methods (BEM). Haug et al. (2018) described this approach assumes an ideal fluid environment characterized by inviscid (dynamic viscosity, $\mu = 0$), irrotational ($\nabla \times v = 0$), and incompressible fluid properties ($\nabla \cdot v = 0$). This theoretical framework aims to determine the potential velocity function, crucial for analyzing fluid characteristics such as velocity and pressure. The computation of RAOs within BEM techniques was detailed in (Ansys, 2012). Equation (1) expresses the potential velocity, where i, j, and k representing the unit vectors along the x-, y-, and z-axes, respectively, as follows:

$$V = \vec{grad}\ \phi = \nabla_{\phi} = \frac{\partial \phi}{\partial x} i + \frac{\partial \phi}{\partial y} j + \frac{\partial \phi}{\partial z} k \quad (1)$$

The assumption that the fluid remains incompressible, indicating a constant mass within the flow entering and leaving a control surface, formulates the Laplace equation as expressed in equation (2). This equation governs the fluid's motion as described by:

$$\nabla^2{}_{\phi} = \frac{\partial^2 \phi}{\partial x^2} + \frac{\partial^2 \phi}{\partial y^2} + \frac{\partial^2 \phi}{\partial z^2} = 0 \quad (2)$$

When analyzing an FPV system in a wave field, it is crucial to apply suitable boundary conditions at the free surface, seabed, and the FPV body. Equation (3) addresses the seabed boundary condition, crucial for diffraction analysis. Equation (4) represents the impermeability condition of the FPV body, indicating that fluid does not penetrate the body, as shown below:

306

$$\frac{\partial \phi}{\partial z} = 0 \, , with \, z = \, -h_0 \tag{3}$$

307

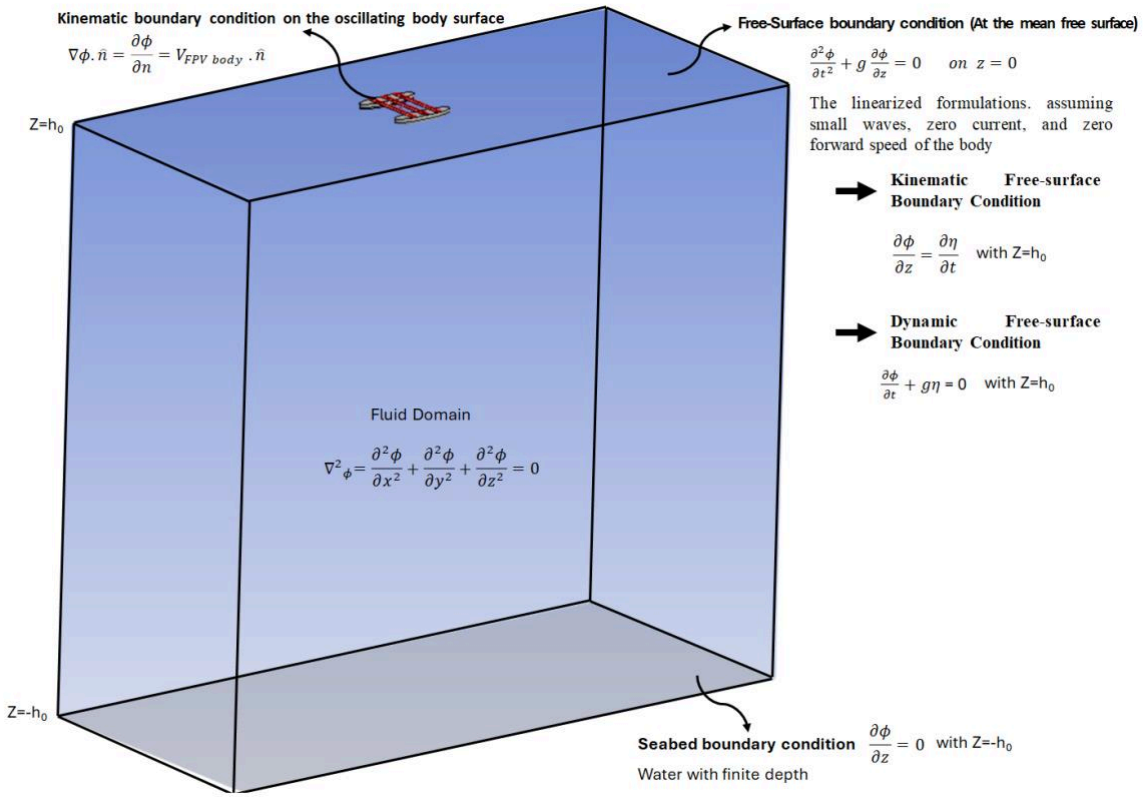
$$\nabla \phi . \hat{n} = \frac{\partial \phi}{\partial n} = V_{FPV \, body} \, . \hat{n} \tag{4}$$

308 Both kinematic and dynamic boundary conditions must be satisfied at the free surface. Linearized
309 conditions are taken about $z = 0$. The kinematic condition ensures the free surface is a streamlined and there is
310 no velocity flux through the surface, while the dynamic condition become equal with the water pressure at the
311 surface to constant atmospheric pressure. Equation (5) provides the linearized formulations for these conditions,
312 assuming small waves, zero current, and zero forward speed of the body, as follows:

313

$$\frac{\partial^2 \phi}{\partial t^2} + g \frac{\partial \phi}{\partial z} = 0 \qquad on \;\; z = 0 \tag{5}$$

314 All relevant boundary conditions in this study concerning BEM 3D Diffraction with Green-Function are
315 depicted in **Figure 6**. These include seabed boundary conditions, free-surface boundary conditions, and kinematic
316 boundary conditions on the oscillating body surface.



317

318 **Figure 6**. Boundary Condition

For a free-floating state of FPV, the wave field generated by the FPV body's motion must be considered. At some distance far away from the FPV body, the potential function must account for the radiating waves from FPV sources.

As elaborated in the previous subsection and consistent with Wei et al. (2024) explanation the panel method is employed to address the hydrodynamics of the floating photovoltaic (FPV) structure (at zero-speed) in the waves field. The propagation of incident waves influences the isolated space-dependent potential component (ϕ), which can be separated into contributions from the incident wave potential (ϕ_i), the radiation wave potential (ϕ_r), and the diffraction wave potential (ϕ_d), as outlined in the equation (6) as follows:

$$\phi = \phi_i + \phi_r + \phi_d \tag{6}$$

ϕ_i, ϕ_r, ϕ_d representing the potential functions for the incident wave, radiation wave, and diffraction wave, respectively. ϕ_i is computed using Airy linear theory, while the derivation of ϕ_r and ϕ_d relies on the application of diffraction theory. In diffraction theory, the potential function is determined by solving the Laplace equation, considering relevant boundary conditions, and subsequently calculating the pressure and resulting forces acting on the body. Additionally, pressure is extracted using the Bernoulli equation, and the potential function is determined as following equation (7), as follows:

$$p = -\rho g z - \rho\left(\frac{\partial \phi_i}{\partial t} + \frac{\partial \phi_r}{\partial t} + \frac{\partial \phi_d}{\partial t}\right) \tag{7}$$

In conclusion, the integration of pressure over the entire wet surface area produces wave excitation forces, which are then utilized in the AQWA software.

4.3. Seakeeping Equation

In the following step, within equation (8), the linearization of the incident wave velocity potential is described as the result of originally solving regular waves. Irregular waves can be conceptualized as a superposition of infinitely linear regular waves. According to the linear potential flow theory and employing the variable separation method, the planar incident velocity potential can be formulated using the following expressions (8) – (9), detailed below:

$$\Phi_I(x, y, z, t) = Re\{\phi_i(x, y, z)e^{-iwt}\} \tag{8}$$

$$\phi_I(x,y,z) = -\frac{A.g}{w}\frac{\cosh k\,(z+h)}{\cosh kh}\; e^{ik(x\cos\beta + y\cos\beta)} \tag{9}$$

345 The variables in equation (9) are defined as follows: A represents the wave amplitude (m), k denotes the
346 wave number, β signifies the wave incident angle (°), h stands for the water depth, and g represents the
347 gravitational acceleration. From the boundary conditions in free surface can then be derived from equation (10)
348 as dispersion relationship for linear theory wave, as detailed in the following:
349

$$w^2 = g\; k \tanh kh \tag{10}$$

350 The method utilized the green function to compute both the radiation and diffraction potentials as described
351 by (Guha, 2016). This method, also known as the BEM, operates on the principle of determining the function G
352 instead of directly solving the equations. By distributing source points across a finite number of grids on the
353 discretized boundary, control points are arranged within each mesh to simultaneously fulfill the boundary
354 conditions. This arrangement establishes the surface source intensity. Once the surface conditions are determined,
355 the surface source intensity is resolved, enabling the computation of both the radiation velocity potential and the
356 diffraction velocity potential. This approach allows the velocity potential in the flow field to be expressed as the
357 integral of G along the body surface boundary of the floating object as following equations (11) – (12):
358

$$\varphi_R(\mathrm{P}) = \sum_{j=1}^{N} \frac{1}{4\pi} \int_{\Delta S_j} \sigma_r(Q)\; \mathrm{G}\;(\mathrm{P},Q)\, dS \tag{11}$$

359

$$\varphi_D(\mathrm{P}) = \sum_{j=1}^{N} \frac{1}{4\pi} \int_{\Delta S_j} \sigma_d(Q)\; \mathrm{G}\;(\mathrm{P},Q)\, dS \tag{12}$$

360 Following this, the equations for computing forces and determining RAO will be derived from Green
361 Function. The wave excitation force, considering both incident and diffracted waves, is expressed through the
362 following equations (13) – (14):
363

$$F_d^{(1)} = \int \int_{\Delta S_j} i\rho\omega \left(\phi_i^{(1)} + \phi_d^{(1)}\right) e^{i\omega t}\; n_i{}'\, dS \tag{13}$$

$$F_r^{(1)} = \int \int_{\Delta S_j} i\rho\omega \left(\sum_{j=1}^{6} \eta_j^{A(1)} \phi_j^{*(1)} \right) e^{i\omega t}\, n_i{}' dS \tag{14}$$

$for\ i = 1 \sim 6$

Where $\vec{n}' = (n_1{}', n_2{}', n_3{}')$ for translational motion and $\vec{r} \times \vec{n}' = (n_4', n_5', n_6') = (yn_3' - zn_2'\,; zn_1' - xn_3'\,;\ xn_2' - yn_1')$

Finally, this equation is essential for determining the RAO related to the system's motion of floating object. The equation used to calculate the motion RAO is presented in Equation (15) below:

$$\sum_{j=1}^{6} \left[-\omega^2 \left(M_{ij} + M_{ij}^{ad} \right) + i\omega B_{ij} + C_{ij} \right] \eta_j^{A(1)} = \int \int_{\Delta S_j} i\rho\omega \left(\phi_i^{(1)} + \phi_d^{(1)} \right) n_i{}' dS \tag{15}$$

Where M_{ij} is vessel mass matrix, M_{ij}^{ad} is vessel added mass matrix, B_{ij} is radiation damping coefficient, C_{ij} = hydrostatic stiffness coefficient, η_j= jth vessel motion amplitude in jth mode motion, $n_i{}'$ denotes the unit normal pointing outward from the floating object surface.

Finally RAO is a function of the dynamic motion of a structure induced by waves within a specific frequency range. RAO serves as a tool to convert wave forces into the dynamic motion response of the structure. Translation and rotational RAOs are defined by Equations (16) and (17) respectively, as shown below:

$$RAO_{(k=x,y,z)} = \frac{\zeta_{k0}}{\zeta_0} \tag{16}$$

$$RAO_{(k=\theta,\phi,\psi)} = \frac{\zeta_{k0}}{\left(\frac{\omega^2}{g}\right)\zeta_0} \tag{17}$$

4.4. Irregular Wave Spectrum

The random ocean wave is characterized by an energy density spectrum, which describes the energy content of the wave and its distribution across a frequency range (Chakrabarti, 2005). This wave energy spectrum is crucial for understanding the behavior of random waves, particularly in the context of designing FPV systems. The method of designing with random waves is essential as it accounts for the inherent variability and unpredictability of ocean conditions. Typically, random waves are described using their statistical parameters, providing a more comprehensive and realistic approach to design compared to deterministic wave models. Therefore, a study on wave spectral sensitivity was conducted using several spectral equations, including the Pierson-Moskowitz and

JONSWAP spectra with peak enhancement factors (γ) ranging from 2.0 to 3.3. Additionally, wave spectral formulations such as ITTC and ISSC were employed to enhance the sensitivity analysis of the motion response to various wave energy conditions.

4.4.1. Modified Pierson Moskowitz and JONSWAP

The Pierson-Moskowitz (PM) spectrum, established by Pierson & Moskowitz (1963), provides a comprehensive description of a fully developed sea in deep water and unlimited wind-generated fetch ocean. This condition is characterized by wind blowing consistently for an extended period (6-18 hours) over a fetch length of 200-600 km, allowing the ocean surface to achieve a steady state. The PM spectrum is empirically derived, with the wind speed, U_w, measured at a height of 19.5 m above mean sea level, serving as the single parameter defining the energy spectrum. Thus, to address specific spatial ocean areas and fresh wind seas, Bretschneider (1952, 1963) developed a two-parameter version of the PM spectrum, utilizing significant wave height and peak frequency. This modified PM or Bretschneider spectrum is comprehensively detailed in (Lewis V, 1988). Then, for the Joint North Sea Wave Program, a major international study conducted off the island of Sylt in the German Bight with offshore winds, resulted in the development of the JONSWAP (Joint North Sea Wave Project) spectrum (Hasselmann et al., 1973). The JONSWAP spectrum is more peaked than the Pierson-Moskowitz (P-M) and Bretschneider spectra, reflecting a more accurate representation of wave energy distribution in the North Sea. This spectrum incorporates modifications to the P-M spectrum to better accommodate the characteristics of ocean waves. According to various studies, it is advisable to use a smaller γ parameter, typically around 2.0 to 2.5, for Indonesian waters (Djatmiko, 2012). This adjustment aims to reduce the dominance of energy contributed by specific wave frequencies, making the JONSWAP spectrum suitable for application in Indonesia's archipelago. The recommended parameters and equations for this application, based on Det Norske Veritas (2010), are provided in equations (18) – (22) as follows:

$$S_J(\omega) = A_\gamma S_{PM}(\omega)\gamma^{exp\left[-0.5\left(\frac{\omega-\omega_0}{\sigma\omega_0}\right)^2\right]} \tag{18}$$

$$S_{PM}(\omega) = \frac{5}{16}.{H_s}^2{\omega_0}^4.\omega^{-5}exp\left[-\frac{5}{4}\left(\frac{\omega}{\omega_0}\right)^{-4}\right] \tag{19}$$

$$\omega_0 = \frac{0.161g}{H_s} \tag{20}$$

$$A_\gamma = 1 - 0.287 \ln(\gamma) \tag{21}$$

411

$$\sigma = 0.07 \text{ for } \omega \leq \omega_0 \tag{22}$$

or $\sigma = 0.09$ for $\omega > \omega_0$

412 Where, $S_J(\omega)$ is the JONSWAP spectrum, $S_{PM}(\omega)$ is the Pierson-Moskowitz spectrum, ω_0 is the peak frequency,
413 g is the gravitational acceleration, H_s is the significant wave height, A_γ is the normalizing factor, γ is the non-
414 dimensional peak shape parameter, and σ is the spectral width parameter.

415 **4.4.2. ITTC - 1975**

416 At the 14th International Towing Tank Conference (ITTC) held in Ottawa, Canada, in 1975, Mirokhin and
417 Kholodilin proposed a new formula for wave spectra, incorporating the latest data available at the time (ITTC,
418 1975). Hydrodynamics experts from various laboratories worldwide, affiliated with ITTC, participated in this
419 conference. This formulation was widely accepted as the fundamental standard for various ship motion testing in
420 random waves. Consequently, ITTC collaborated with the International Ship and Offshore Structures Congress
421 (ISSC), and both organizations decided to adopt the recommended formulation. Thus, this formulation became
422 known as the ITTC/ISSC spectrum (ITTC, 2023), represented by equation (23) as shown below:

423

$$S_{ITTC}(\omega) = \frac{0.0081 \,.\, g^2}{\omega^5} \times \exp\left(\frac{-3.11}{{H_s}^2 . \omega^4}\right) \tag{23}$$

424 Where $S_{ITTC}(\omega)$ is the ITTC wave spectrum, ω is the wave frequency, g is the gravitational acceleration, H_s is
425 desired the significant wave height.

426

427 **4.4.3. ISSC - 1964**

428 Bhattacharyya (1978) explained that the International Ship Structure Congress (ISSC) in 1964 established
429 recommendations for using a spectrum equation that is a slight modification of the Bretschneider spectrum (1959).
430 This equation incorporates two variables: the significant wave height, denoted H_s and the mean frequency, $\bar{\omega}$. The
431 recommended formulas are given as equations (24) and (25) as detailed below:

432

$$S_{ISSC}(\omega) = 0.1107 . {H_s}^2 . \frac{\bar{\omega}^4}{\omega^5} \times \exp\left[-0.4427 \left(\frac{\bar{\omega}}{\omega}\right)^4\right] \tag{24}$$

$$\bar{\omega} = 1.296 \,.\, \omega_0 \tag{25}$$

4.5. Spectral Response Structure

The responses of a floating structure in irregular waves shall be obtained by correlating the RAO with the wave spectrum within transforming wave energy into response energy with the following equation (26). Subsequently, the amplitude significant response is calculated as equation (27) as follows:

$$S_{\zeta r}(\omega) = RAO^2 \times S_{\zeta}(\omega) \tag{26}$$

$$\zeta_s = 2\sqrt{m_0} \tag{27}$$

Where $S_{\zeta r}$ (ω) is the response spectrum, S_{ζ} (ω) is the waves spectrum and m_0 is the area under the response spectrum curve as shown in the following equation (28) and detailed in equation (29), as follows:

$$m_0 = \sum_{n=1}^{\infty} S_{\zeta}(\omega)\delta\omega = \int_0^{\infty} S_{\zeta}(\omega)d\omega \tag{28}$$

$$m_0 = \frac{1}{3} \times \Delta\omega \times \Sigma_0 \tag{29}$$

The sum of Σ_0 as the baseline for calculating the area under the response spectra curve. This calculation will be performed by applying Simpson's rule and factoring in the frequency increment within a particular interval of second wave frequencies minus with first wave frequencies, Δω.

4.6. 3-D Diffraction Numerical Setup

The three-dimensional (3D) models of FPV were developed using dynamic 3D modelling software and were exported in .step format to conduct seakeeping analysis using AQWA. Then, there are three analysis stages are required to calculate the hydrodynamics FPV using AQWA as depicted in the following **Figure 7**.

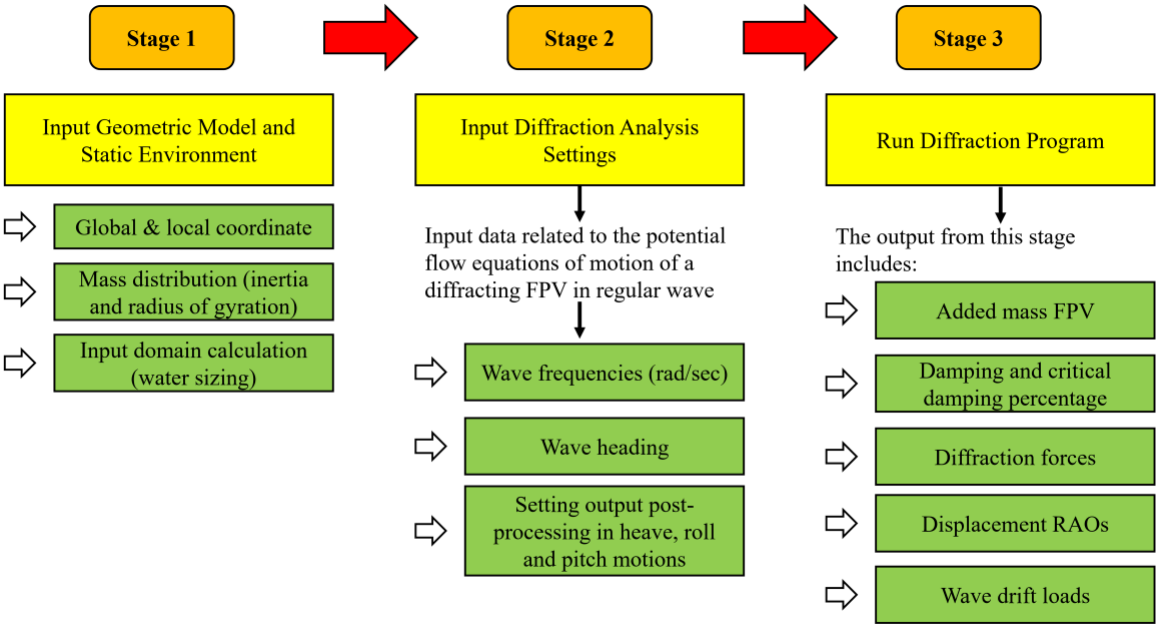
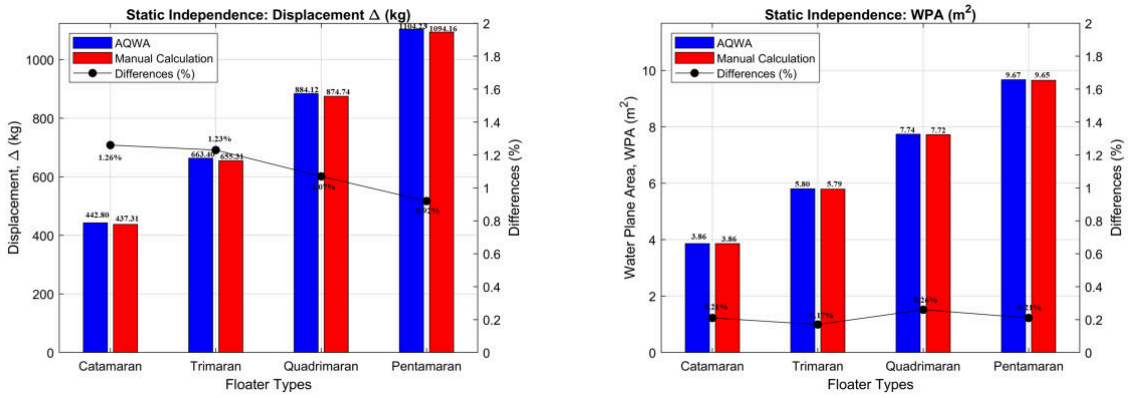


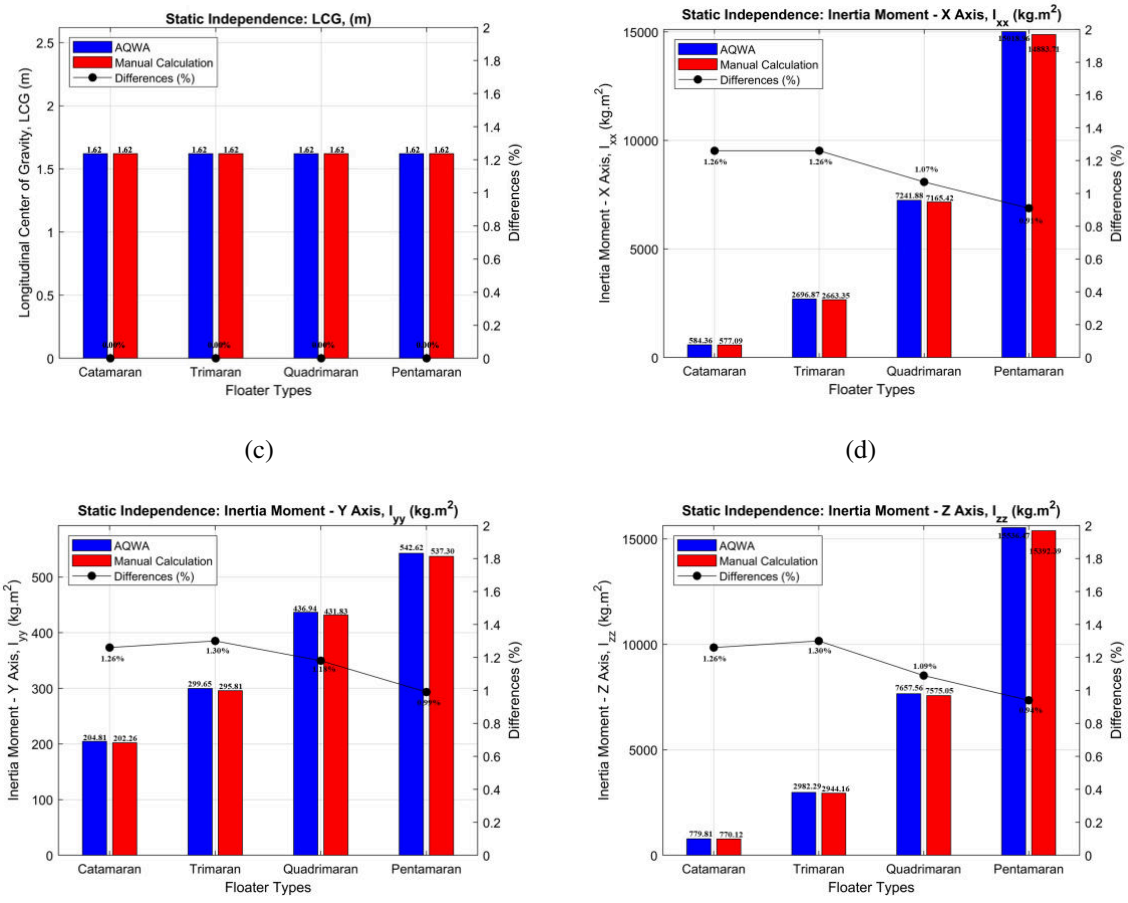
Figure 7. Stages of AQWA numerical analysis, redrawn from (Ansys, 2012)

4.6.1. Grid Independency Studies (GIS)

Grid independence studies involve two types: static and dynamic independence. For static independence, a comparison between AQWA-hydrostatic results and the baseline of manual calculations was conducted, with the requirement that the results remain within a 2% threshold for all considered parameters, including hydrostatic and mass inertia properties. The detailed results, as recommended by Suastika et al. (2021), are presented in **Figure 8 (a) – (f).** The figures illustrate that the primary Y-axis (left) displays various hydrostatic parameter values, with the AQWA model represented by blue bars and manual calculations by red bars. Additionally, a line chart indicates the error percentage, showing the differences between the AQWA model and manual calculations. The error percentages are marked by the secondary Y-axis (right).



(a) (b)



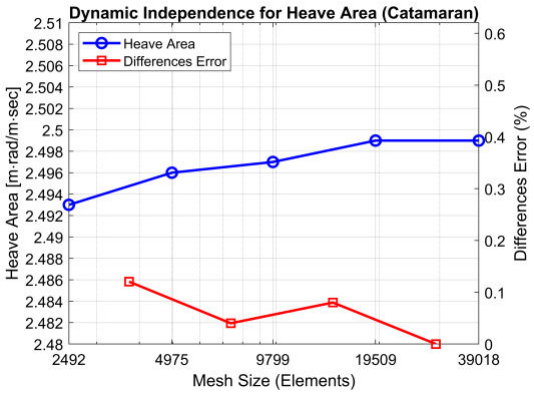
(c) (d)

(e) (f)

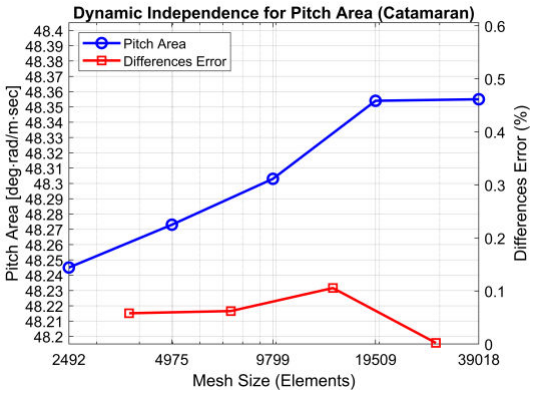
Figure 8. Static independence parameters: (a) displacement, (b) water plane area, (c) longitudinal center of gravity, (d) inertia moment, x-axis, (e) inertia moment, y-axis, (f) inertia moment, z-axis

Furthermore, dynamic independence in diffraction systems involves conducting simulations to compute the area under the RAO graph across wave frequencies for specific motions while utilizing varying grid resolutions. Improving simulation precision requires deploying finer grid resolutions around the model to capture interaction phenomena accurately. This strategic mesh arrangement optimizes computer performance while enhancing result accuracy. The grid analysis encompassed two types of motion: translational (global-Z) and rotational (global-RY), as shown in **Figure 9 (a) – (h).**

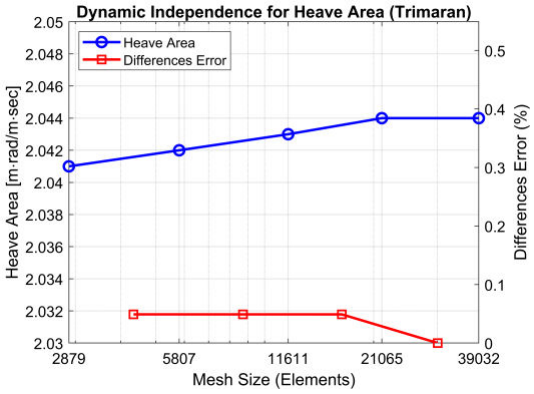
The figures consist of two lines, blue and red. The blue line represents the parameter values considered in dynamic independence for each mesh size variation and corresponds to the primary Y-axis (left). The red line indicates the differences in parameter values between the two considered mesh sizes, shown as percentage error, and corresponds to the secondary Y-axis (right).


Dynamic Independence for Heave Area (Catamaran)
Heave Area
Differences Error
Heave Area [m·rad/m·sec]
Differences Error (%)
Mesh Size (Elements)
2492
4975
9799
19509
39018

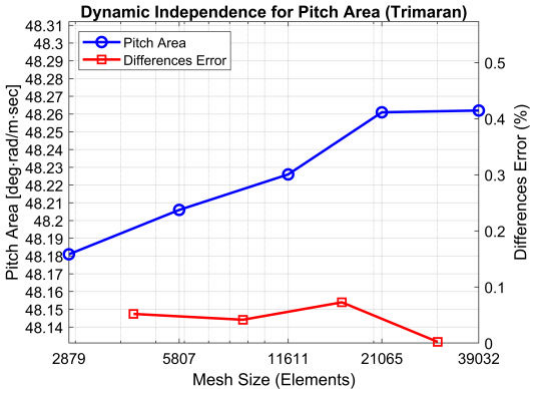
(a)


Dynamic Independence for Pitch Area (Catamaran)
Pitch Area
Differences Error
Pitch Area [deg·rad/m·sec]
Differences Error (%)
Mesh Size (Elements)
2492
4975
9799
19509
39018

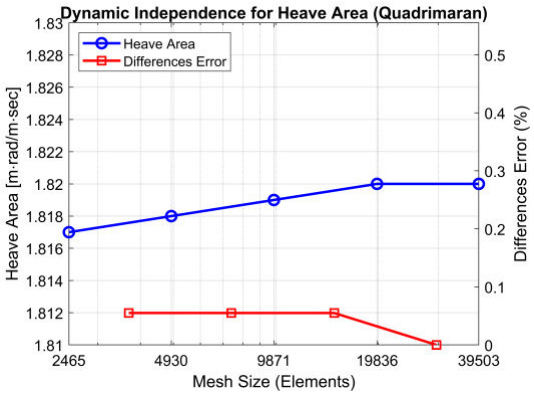
(b)


Dynamic Independence for Heave Area (Trimaran)
Heave Area
Differences Error
Heave Area [m·rad/m·sec]
Differences Error (%)
Mesh Size (Elements)
2879
5807
11611
21065
39032

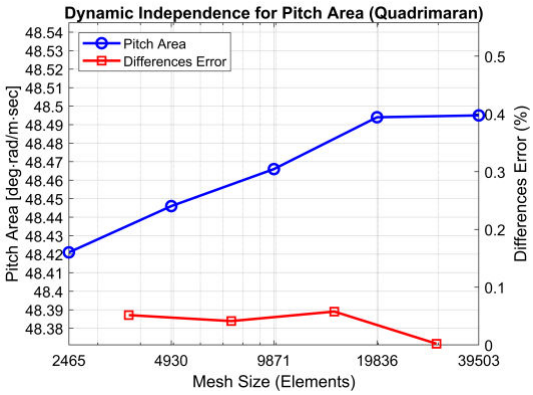
(c)


Dynamic Independence for Pitch Area (Trimaran)
Pitch Area
Differences Error
Pitch Area [deg·rad/m·sec]
Differences Error (%)
Mesh Size (Elements)
2879
5807
11611
21065
39032

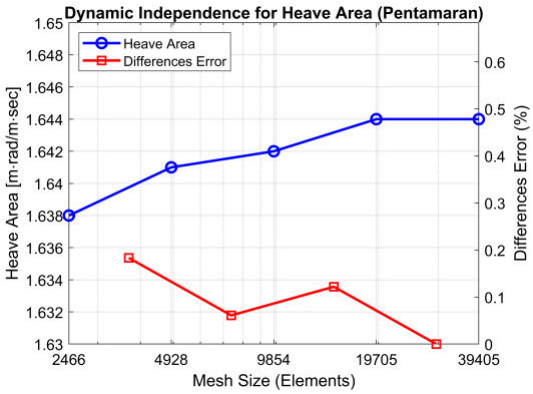
(d)


Dynamic Independence for Heave Area (Quadrimaran)
Heave Area
Differences Error
Heave Area [m·rad/m·sec]
Differences Error (%)
Mesh Size (Elements)
2465
4930
9871
19836
39503

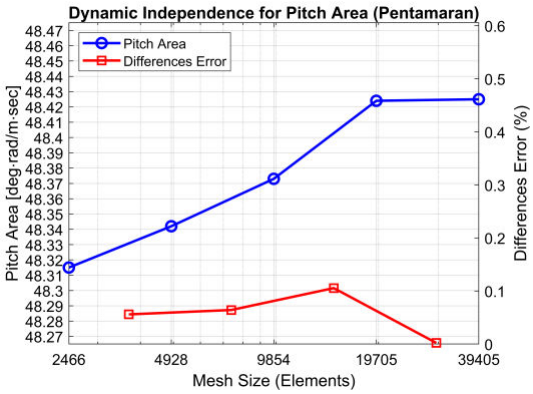
(e)


Dynamic Independence for Pitch Area (Quadrimaran)
Pitch Area
Differences Error
Pitch Area [deg·rad/m·sec]
Differences Error (%)
Mesh Size (Elements)
2465
4930
9871
19836
39503

(f)



(g)



(h)

Figure 9. Dynamic independence parameters: (a-b) Catamaran, (c-d) Trimaran, (e-f) Quadrimaran, (g-h) Pentamaran

4.6.2. Mass moment of inertia distribution

These values, which align with those computed using dynamic 3D modeling software (see Section 4.1), are detailed in **Table 6**. The FPV model incorporates mass characteristics through a point mass and mass moments of inertia, defined by the radii of gyration, as presented in equation (30) as follows:

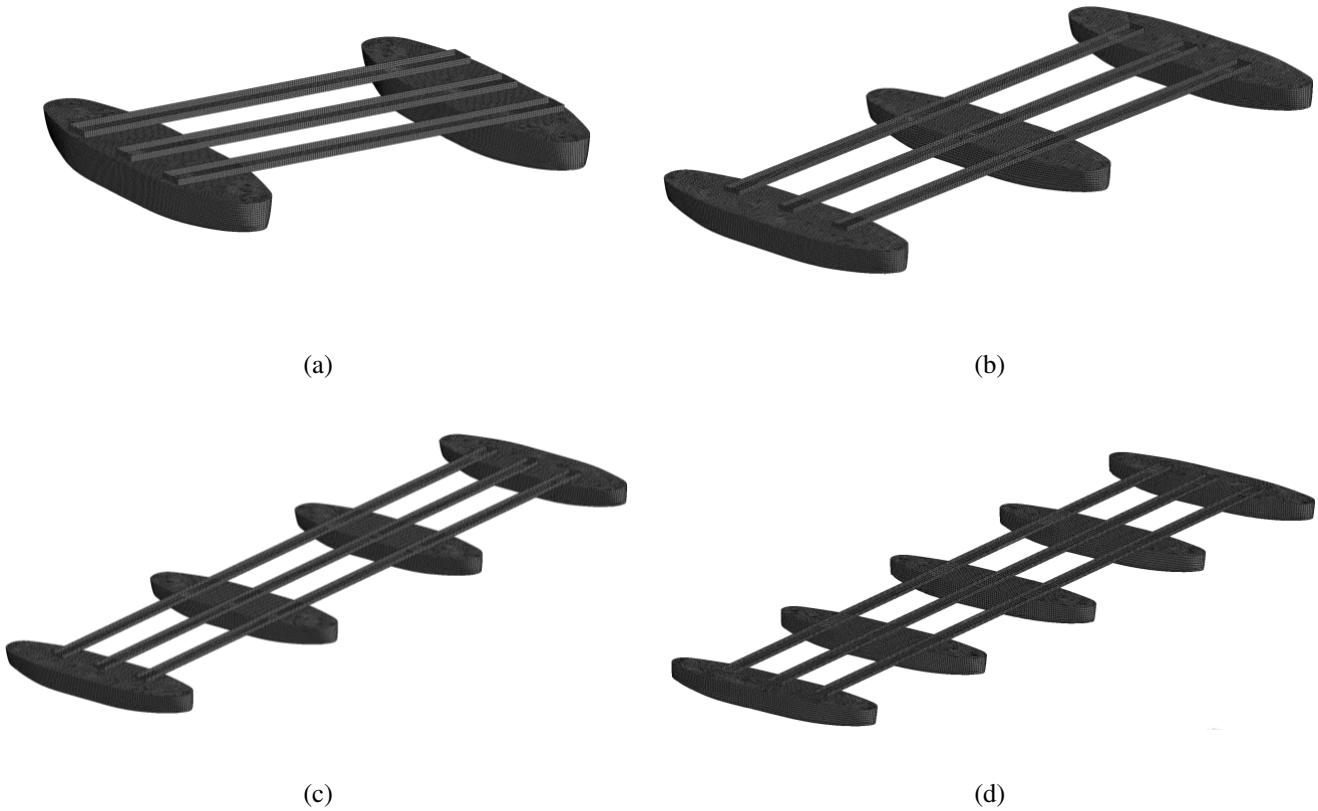
$$k_{ii} = \sqrt{\frac{\sum I_i}{\sum w_i}} \tag{30}$$

Where k_{ii} is radius of gyration of FPV, I_i is the inertia moment of FPV, and w_i is the mass distribution along the discretization point, i denotes in a specific axis. The intersection of the three symmetry planes of the multihull configuration, shown in **Figure 4**, served as the reference point designated as (0,0,0) at the centre line of the FPV body in Aft Perpendicular (AP). This point was used to reference the offsets of the global centre of gravity (CoG).

Table 6. Radii of gyration of FPV

Component	unit	K_{xx} (X-Axis)	K_{yy} (Y-Axis)	K_{zz} (Z-Axis)
Catamaran	m	1.15	0.68	1.33
Trimaran	m	2.02	0.67	2.12
Quadrimaran	m	2.86	0.70	2.94
Pentamaran	m	3.69	0.70	3.75

Calculations of pressures and forces on each numerical element discretization in the hull surface geometry are provided by the generated mesh within the diffraction system (Bosma et al., 2012). A fine mesh was employed for the entirety of the FPV models, as depicted in **Figure 10**.



(a) (b)

(c) (d)

Figure 10. Mesh vizualization: (a) Catamaran, (b) Trimaran, (c) Quadrimaran, (d) Pentamaran

Additionally, visualizations of the progressive mesh sizes are included in **Figure 11**, focusing specifically on the catamaran model as a representative example. It is important to emphasize that higher mesh quality enhances the discretization process, especially in regions with complex body curvature. Inadequate discretization in panel methods can impact numerical simulations.

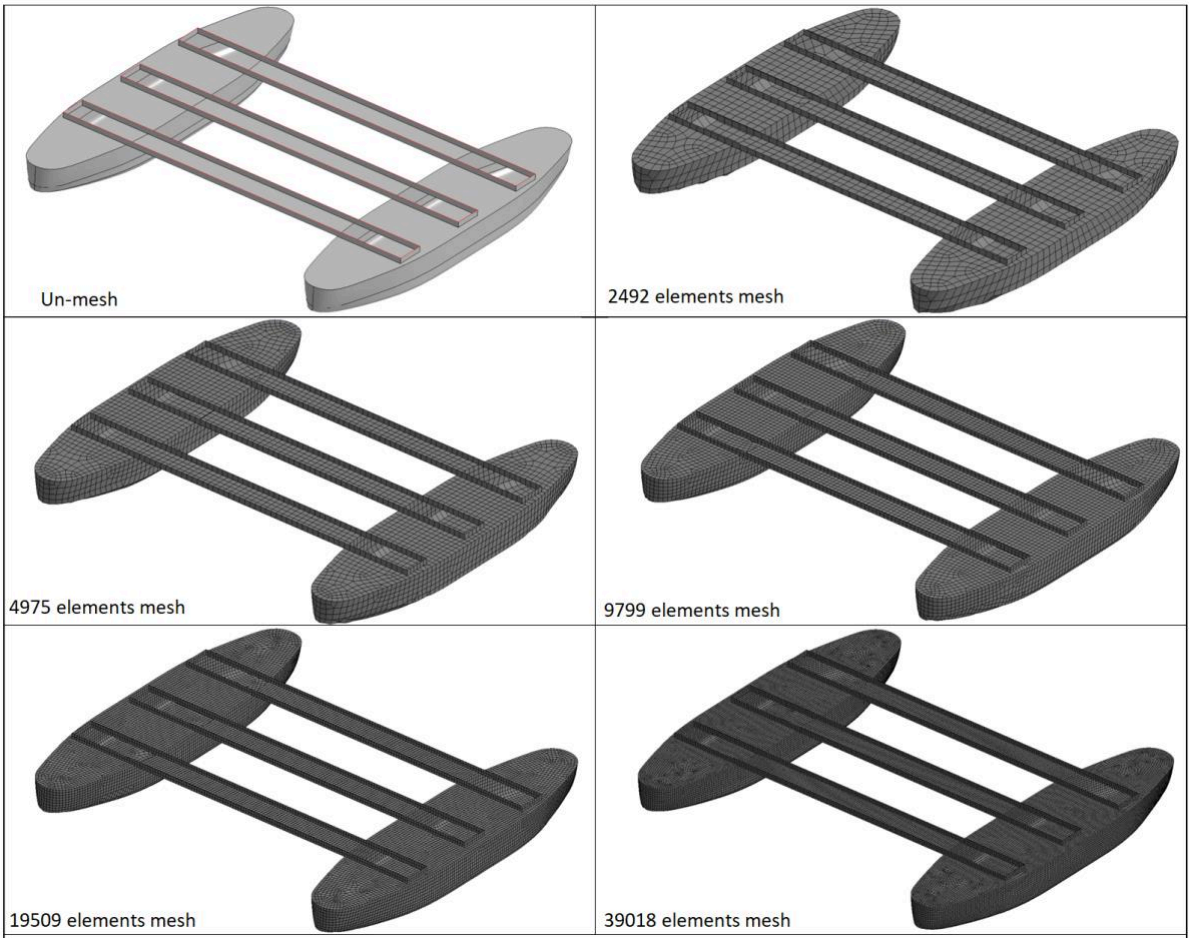


Figure 11. Progressive mesh sizes

5. Result and discussion

The results and discussion in this paper are structured into several subsections: structural motion and the sensitivity of wave spectra at different sea states, including the FPV response spectra of the structure. 3-D surface plots within the extension file .xyz illustrate the quality of motion response for each natural oscillatory mode, providing a comprehensive visualization of the dynamic behaviour of the FPV system. Various wave spectra are applied and combined with several proposed design components, ranging from catamaran to pentamaran configurations, to show the relationship between the influences of FPV floating structure geometries and their sensitivity to wave spectra at specific water locations – sea-state. The section presents comprehensive findings of these objectives.

The analysis of FPV structures involves considering wave propagation to capture the dynamic behavior caused by hydrodynamic loads. This analysis includes head seas ($\varphi = 0°$), quartering seas ($\varphi = 45°$), and beam seas ($\varphi = 90°$), as shown in **Figure 12**. This consideration results from the symmetrical geometry of the stern and bow in all the proposed designs. Consequently, wave loads on one heading produce identical responses on the opposite heading due to this symmetrical plane.

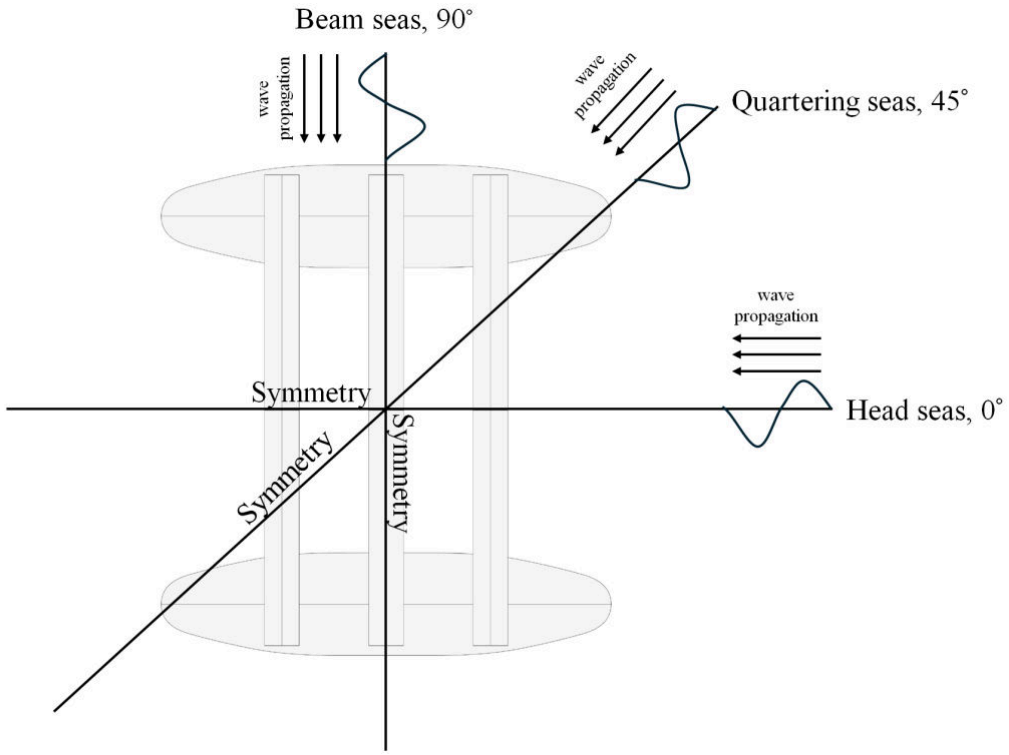


Figure 12. Wave heading

5.1. Structural motion in regular waves

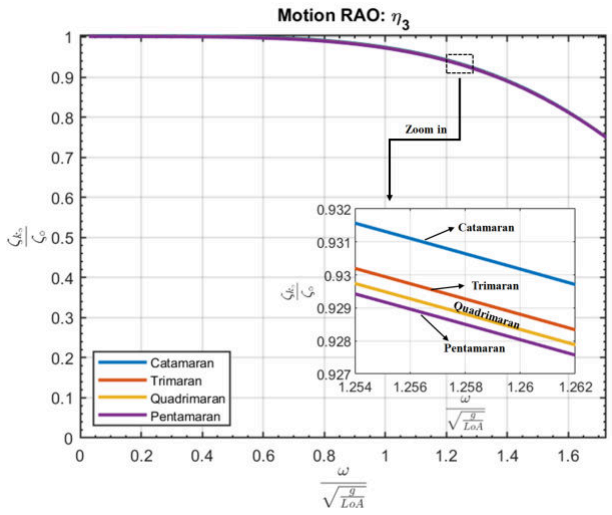
The motion analysis graphs for each heave, roll, and pitch mode of the proposed design model have been detailed in the frequency range (ω) of 0.05 - 3.00 rad/sec. Heave RAO graphs are examined for headings φ = 0°, φ = 45°, and φ = 90°. Roll RAO graphs are analysed for headings φ = 45° and φ = 90°, whilst pitch RAO graphs are evaluated for headings φ = 0° and φ = 45°.

5.1.1. Heave motion

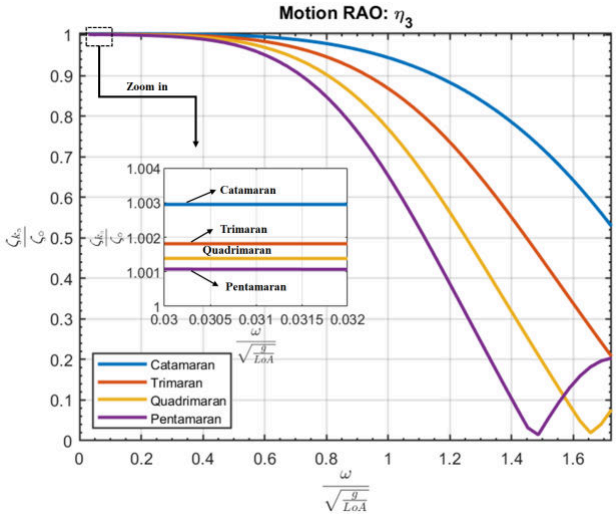
The analysis of the graphs reveals that at a 0° wave heading, all hull designs perform similarly in regular waves, with the pentamaran exhibiting the lowest response. Generally, the heave motion remains consistent as the hulls move together when waves comes from the forward (FP) or aft position (AP), due to their side-by-side configuration. The heave response reaches its peak in following or head seas (φ = 0° / 180°), with waves from behind causing increased vertical motion in the FPV. This observation supports findings by (Murdijanto et al., 2011).

Figure 13 (a) – (c) shows that the heave response of the catamaran model under all wave headings exhibits relatively conservative motion. The addition of hull configurations results in damping effects on the structure,

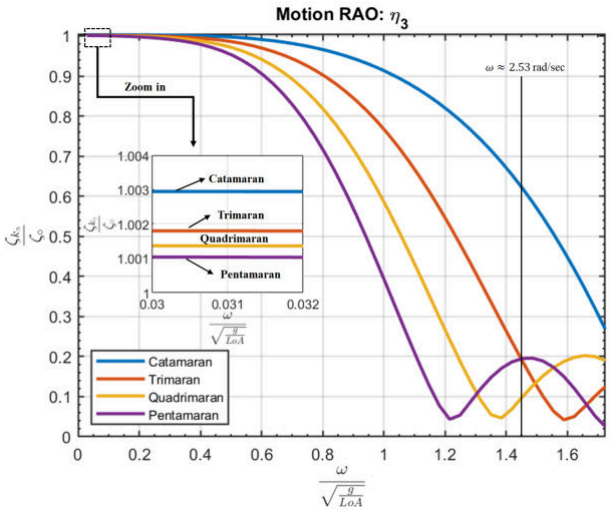
shifting the curve towards lower wave frequencies (long waves) with a significant decrease. At a regular wave frequency, $\omega \approx 2.53$ rad/sec or $\left(\frac{\omega}{\sqrt{\frac{g}{\mathrm{LoA}}}} \approx 1.45\right)$, particularly at a beam seas ($\varphi = 90°$) wave heading, reveal that the catamaran model shows a heave response of approximately $\frac{\zeta_{k_0}}{\zeta_0} \approx 0.62$. This response decreases in the trimaran model to $\frac{\zeta_{k_0}}{\zeta_0} \approx 0.19$ and further decreases in the quadrimaran model to $\frac{\zeta_{k_0}}{\zeta_0} \approx 0.10$. However, the pentamaran model exhibits a slight increase to $\frac{\zeta_{k_0}}{\zeta_0} \approx 0.20$, characterized by a peak followed by a decrease in the motion pattern. This behaviour is attributed to hydrodynamic interactions among the multiple hulls of the pentamaran. Specifically, the interaction of fluid between the hulls creates strong resonant effects. As noted by Chen et al. (2021), this is due to the limitations of potential flow theory, which does not account for viscosity and energy dissipation. This limitation can lead to unrealistic wave resonances in the gaps between adjacent hulls. Complex wave patterns with multiple crests may appear when these gaps are large. These observations are consistent with the findings of Tajali & Shafieefar (2011), which indicates that heave transfer functions (RAO) exhibit similar patterns in multi-body floating structures.



(a)



(b)



(c)

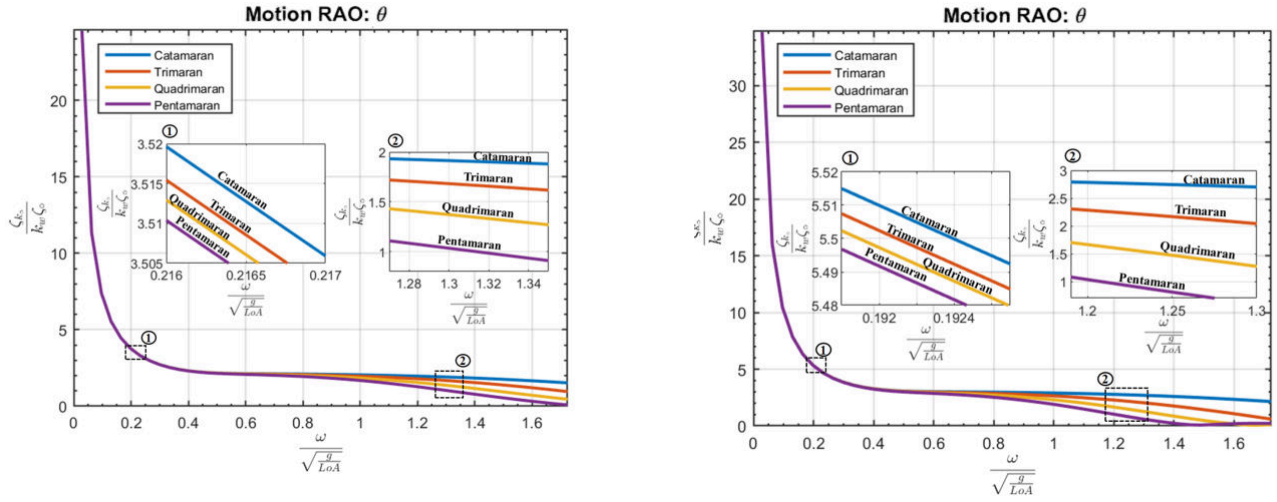
Figure 13. Global-Z (η_3) transfer function based on wave heading: (a) φ = 0°, (b) φ = 45°, (c) φ = 90°

5.1.2. Roll motion

Further analysis of roll response, as illustrated in **Figure 14 (a) – (b)**, indicates that wave heading, φ = 90° (beam seas) plays a crucial role in generating more conservative roll motions compared to wave heading, φ = 45° (quartering seas). This observation aligns with the study by Pacuraru et al. (2020) which explains that beam seas cause the vessel to move more extremely from side to side, a motion known as roll, and roll motion is highly sensitive to beam sea conditions. As the vessel moves further from the beam waves, the roll motion of the ship decreases.

The graphs demonstrate that increasing the number of hulls results in a substantial reduction in maximum roll response for both wave headings (φ = 45° and 90°). As the wave propagation shifts towards beam seas, the gap distance of each line in the graph between configurations widens, indicating the increasing impact of hull configuration on roll reduction, which is related to the increase in damping.

The study by Bhattacharyya (1978) and Zhao et al. (2023) supports these findings. They identified that increasing the number of hull configurations enhances the metacentric height, leading to a notable reduction in excitation force due to roll motion. This reduction is related to the natural period of motion, lateral acceleration, and improved transverse stability. This finding is also relevant to the work of Tajali & Shafieefar (2011), who explains that an increase in the mass of the floating structure and its structural width (as seen in this study with the addition of more hulls) leads to a reduction in motion amplitude.



(a) (b)

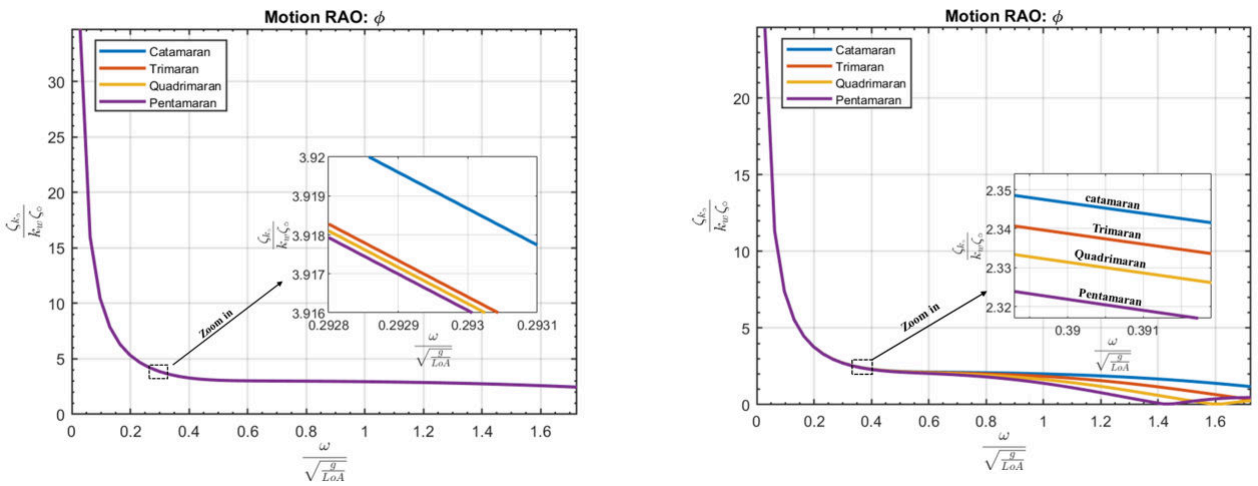
Figure 14. Global-RX (θ) transfer function based on wave heading: (a) φ = 45°, (b) φ = 90°

5.1.3. Pitch motion

Several key points arise from the graphs in **Figure 15 (a) – (b)**. In the pitch motion mode, all proposed designs exhibit identical responses when regular waves impact the structure from a φ = 0° heading (head or following seas), with the pentamaran consistently showing the lowest response. This occurs because all models consistently provide identical response values throughout the specified wave frequency range when stimulated by waves from the dominant pitch motion direction (φ = 0°). This indicates that adding hull configurations to the FPV structure does not significantly influence performance (Jifaturrohman et al., 2024).

The graphs show that pitch motion (RY-axis) is dominated by wave headings at φ = 0° or 180°, with the Y-axis peaks occurring during following/head seas. These peaks are 41.2% higher than those observed in quartering seas (φ = 45°).

However, significant differences appear at a φ = 45° wave heading, where the catamaran model shows a more conservative pitch motion. The effect of adding hull configurations side-by-side as shown by the widening gap into lower response between the model configuration lines in the graph, indicates improved motion stability.



(a) (b)

Figure 15. Global-RY (ϕ) transfer function: (a) φ = 0°, (b) φ = 45°

5.2. Wave spectra and sea-state characterization.

The International Classification Society, American Bureau Shipping, ABS (2016) provides insight into categorizing the continuously changing waves into various sea states, utilizing short-term wave statistics for individual sea state depiction and long-term wave statistics to provide an overview of wave behaviour over extended periods. The fundamental concepts derived from these theoretical advancements include defining a sea state as a spectrum consisting of numerous individual wave components and using spectrum moments to determine parameters like significant wave height (Hs) and peak periods (Tp).

A wave spectrum delineates the energy distribution among wave components of different frequencies within a sea state. While wave spectra can be directly obtained from measured data, mathematical formulations have been developed based on data analysis. These formulations, such as the ISSC Wave Spectrum, Bretschneider Spectrum (also referred to as the Pierson-Moskowitz (P-M) spectrum), JONSWAP spectrum, and ITTC spectrum, provide several analytical methods for wave behaviour characterisation.

Therefore, analysing the wave spectrum is the subsequent process in evaluating the effect of the hull configuration. **Figure 16 (a) – (d)** illustrates several types of wave spectrum in sea states 2–4 for the conservative marine environment in the near-shore application, as seen in **Table 7.**

Sea-state 1 was not considered since its significant wave height (Hs) was too low, resulting in very weak wave energy spectrum values. There is no significant difference among the various types of spectra offered in this research. Hence, a more conservative range of alternatives for spectrum selection is recommended for this study investigation.

Table 7. Sea-State Codes with reference by (Huston, 2010) within maximum range in Hs

Sea-State	Description of sea	Significant Wave Height (m)	Modal Period (s)
2	Smooth (wavelets)	0.50	4.2 – 13.8
3	Slight	1.25	5.1 – 15.4
4	Moderate	2.50	6.1 – 16.2
5	Rough	4.00	7.2 – 16.6

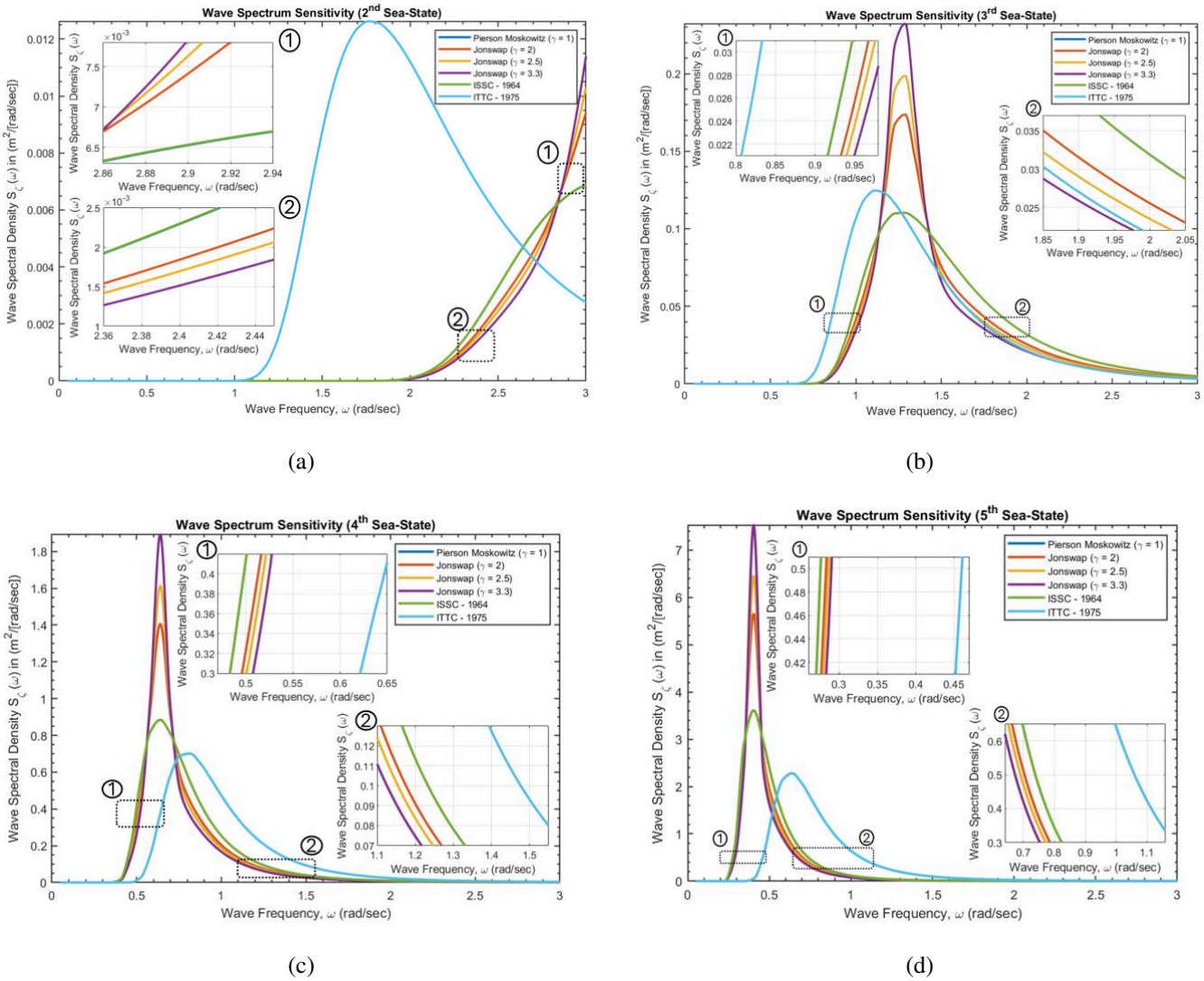


Figure 16. Irregular wave spectrum: (a) H_s = 0.50 m, (b) H_s = 1.25 m, (c) H_s = 2.50 m, (d) H_s = 4.00 m

From **Figure 16**, it can be observed that as the significant wave height (Hs) increases, the peak of the wave spectrum also rises. This peak spectrum is a crucial parameter for generating hydrodynamic excitation forces, which directly affect the motion quality of the FPV in each sea-state condition. As a result, associating the

mathematical equations of each wave energy spectrum with the motion characteristics of the FPV in irregular waves produces stochastic motion quality values that are uniquely relevant to the sensitivity of the given wave energy spectrum.

Figure 16 (a) shows that the ITTC spectrum exhibits a more conservative effect compared to other wave energy spectra. This is due to the ITTC spectrum not being associated with the parameter ω_0, which determines the peak frequency of the generated spectrum. In contrast, the remaining proposed spectra related to the ω_0 parameter have their peak spectrum at an estimated wave frequency of 3.16 rad/sec in sea-state 2.

Figure 16 (b) indicates that the wave energy spectrum curve begins to form more accurately in sea-state 3, with the peak of the spectrum shifting to a wave frequency range of 1.11–1.26 rad/sec. The PM and ISSC spectrum curves are closely aligned, with a difference of only ±0.03% (ABS, 2016; Djatmiko, 2012; ITTC, 2023). Despite the JONSWAP γ=3.3 spectrum having a higher peak, the wave energy generated is slightly lower than the ITTC spectrum, as indicated by the relatively narrower curve of JONSWAP γ=3.3 compared to the wider ITTC spectrum curve, resulting in a difference of approximately ±0.23% in the area under the curve.

Figure 16 (c) demonstrates that all spectra continue to shift towards lower frequencies (longer waves) in the range of 0.63–0.82 rad/sec, with relatively narrower curves compared to previous sea-states. A notable observation is that although the JONSWAP γ=3.3 spectrum has a peak value 2.7 times higher than the ITTC spectrum, the area under the ITTC spectrum curve is 2.24% more conservative compared to the JONSWAP γ=3.3 spectrum. This significantly impacts the root mean square (RMS) motion values for each FPV motion mode.

Lastly, **Figure 16 (d)** shows that the peak spectrum shifts again to a wave frequency range of 0.39–0.64 rad/sec, with even narrower curves, but the peak concentration rises to 3.98 times higher than in the previous sea-state. However, the quantity of wave energy spectra of the PM or ISSC types is more conservative compared to the ITTC or JONSWAP γ=3.3 spectrum, when considering the area under related curves.

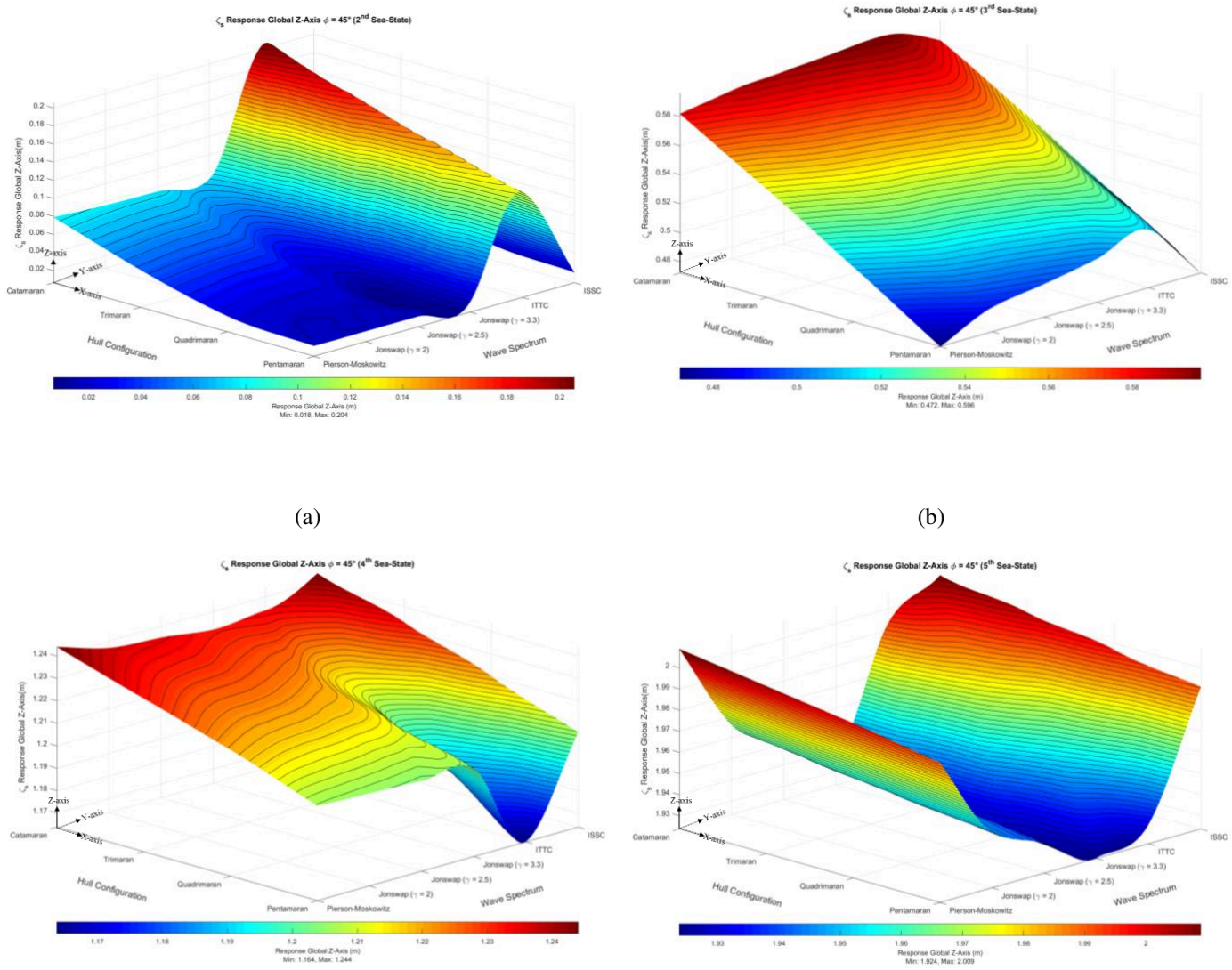
In conclusion, analyzing these figures shows that each wave energy spectrum has distinct characteristics and impacts on the FPV's motion response, highlighting the importance of selecting appropriate spectra for hydrodynamic analysis.

5.3. Significant response amplitude of oscillatory motion in wave sensitivity analysis.

This subsection discusses the relationship between the various wave spectra and several proposed FPV design configurations, focusing on their influence on significant amplitude responses in heave, roll, and pitch motion

modes. The use of 3D surface plots will effectively illustrate the gradient changes for different wave spectral types and design configurations, showcasing the motion quality values as colour gradients.

5.3.1. ζ_s Response Global Z-Axis (η_3) with $\varphi = 45°$



(a) (b)

(c) (d)

Figure 17. ζ_s of heave in wave heading 45° : (a) H_s = 0.50 m, (b) H_s = 1.25 m, (c) H_s = 2.50 m, (d) H_s = 4.00 m

In general, **Figure 17** illustrates that as sea-state conditions become more extreme, the heave motion values increase correspondingly. This is evidenced by the maximum Z value reaching almost 2.01 m for the catamaran model under conservative conditions. Additionally, it can be observed that moving to the right on the X-axis (hull

configurations), the average heave motion values tend to decrease, indicating an improvement in heave motion quality.

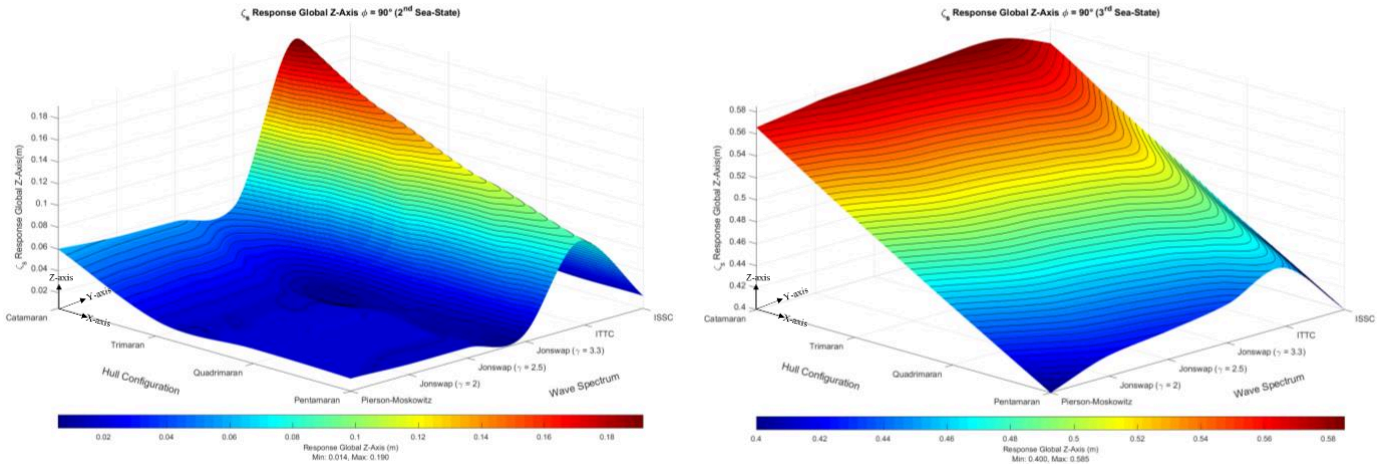
Starting with **Figure 17 (a)**, under the second sea-state condition with Hs = 0.50 m, it can be concluded that the conservative values are observed for the catamaran model with the ITTC wave spectrum. In contrast, other wave spectrum types generate relatively weak heave motions, ranging from approximately 0.02 to 0.08 m, due to insufficient wave energy generation at frequencies below 3 rad/sec.

Figure 17 (b) demonstrates the third sea-state condition with Hs = 1.25 m, here conservative values remain for the catamaran with the ITTC wave spectrum. However, the average heave motion differences among the various wave spectrum types are not significantly different. Additionally, the graph shows a linear negative trend in heave motion values with the addition of hull configurations across all wave spectrum types.

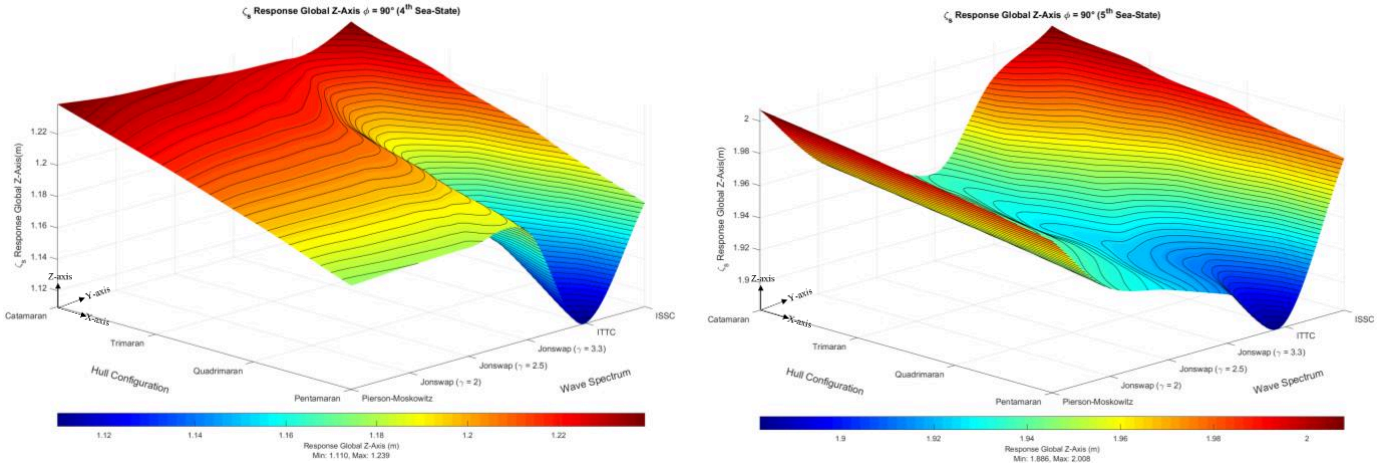
Next, **Figure 17 (c)** illustrates the fourth sea-state condition with Hs = 2.50 m, where the maximum heave motion values are observed for the catamaran configuration but with the PM or ISSC wave spectrum. This is because, in this sea state, the peak spectrum values for PM or ISSC are slightly higher than the ITTC spectrum, resulting in a minor difference in heave motion quality, approximately 0.8%, 1.6%, 2.5% and 3.58% in the catamaran, trimaran, quadrimaran and pentamaran models respectively.

Finally, **Figure 17 (d)** presents the fifth sea-state condition with Hs = 4.00 m, where conservative heave motion values are still found in the catamaran configuration with the PM or ISSC wave spectrum. The lowest values are associated with the JONSWAP γ = 3.3 wave spectrum. This is due to the smaller area under the curve for the JONSWAP γ = 3.3 spectrum compared to the other types.

5.3.2. ζ_s Response Global Z-Axis (η_3) with $\varphi = 90°$



(a) (b)



(c) (d)

669 **Figure 18**. ζ_s of heave in wave heading 90° : (a) H_s = 0.50 m, (b) H_s = 1.25 m, (c) H_s = 2.50 m, (d) H_s = 4.00 m

670

671 **Figure 18** illustrates the impact of significant heave amplitude at a wave heading, φ = 90°. There is no significant
672 difference in the contour pattern, and the values of heave motion amplitude are considerably lower compared to
673 the previous case (φ = 45°).

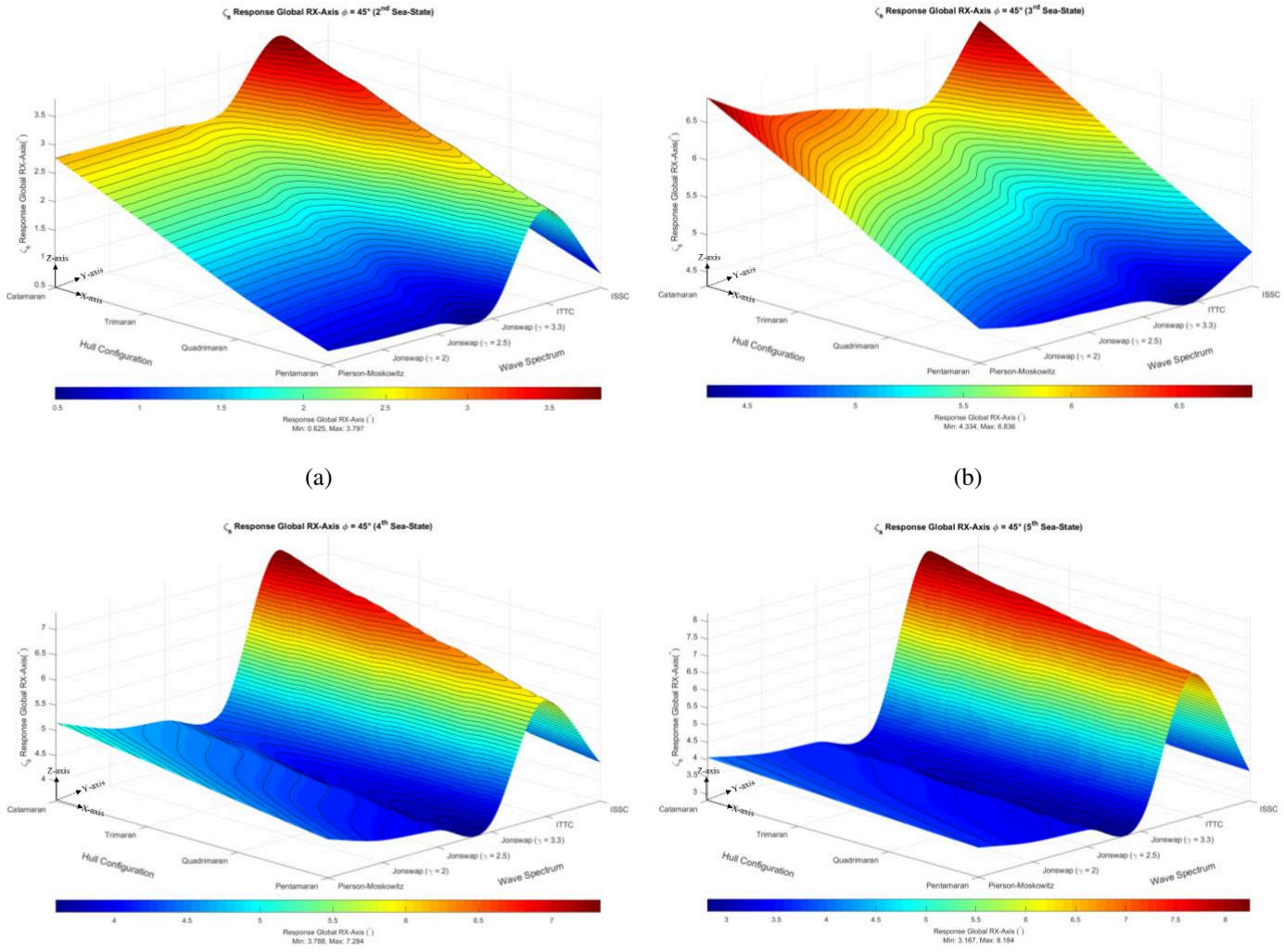
674 Starting with **Figure 18 (a)**, under sea-state 2 conditions, the maximum heave motion is observed in the catamaran
675 configuration with the ITTC wave spectrum, reaching a value of 0.19 m. Higher peak enhancement factor, γ values
676 result in a smaller area under the curve within the wave frequency range of 0.05–3.00 rad/sec. Thus, the contour
677 graph along the Y-axis gradually decreases, then rises again for the ITTC spectrum, and finally declines once
678 more for the ISSC spectrum.

679 **Figure 18 (b)** illustrates sea-state 3 conditions, where the heave motion amplitude ranges from 0.40 to 0.59 m,
680 with the maximum value occurring in the catamaran configuration with the ITTC spectrum. In contrast to the
681 previous sea-state, higher γ values in this scenario correspond to increased heave motion amplitude. This is due
682 to the wave spectrum being fully developed and within the 0.05–3.00 rad/sec frequency range.

683 **Figure 18 (c)** presents sea-state 4 conditions, with the maximum significant heave motion amplitude of
684 approximately 1.24 m observed in the PM or ISSC wave spectrum for the catamaran configuration. The lowest
685 value, around 1.11 m, occurs in the pentamaran configuration with the ITTC spectrum.

Finally, **Figure 18 (d)** illustrates sea-state 5 conditions, where the maximum heave motion reaches 2.01 m in the catamaran configuration with the PM or ISSC spectrum. The lowest amplitude, around 1.89 m, is found in the pentamaran configuration with the JONSWAP $\gamma = 3.3$ spectrum.

5.3.3. ζ_s Response Global RX-Axis (θ) with $\varphi = 45°$



(a) (b)

(c) (d)

Figure 19. ζ_s of roll in wave heading 45°: (a) $H_s = 0.50$ m, (b) $H_s = 1.25$ m, (c) $H_s = 2.50$ m, (d) $H_s = 4.00$ m

Figure 19 illustrates the roll motion quality at a 45° wave heading, indicating that increasing the number of hull configurations in the design generally enhances motion quality. Additionally, analysis of the Y-axis (wave spectrum) shows that a higher γ value correlates with improved roll motion quality in all sea-state conditions. However, a distinct pattern is observed in sea-state 3 with a significant wave height (Hs) of 1.25 m, where the ITTC spectrum indicates a decrease in motion. In contrast, sea-states 2, 4, and 5 exhibit an upward trend in motion.

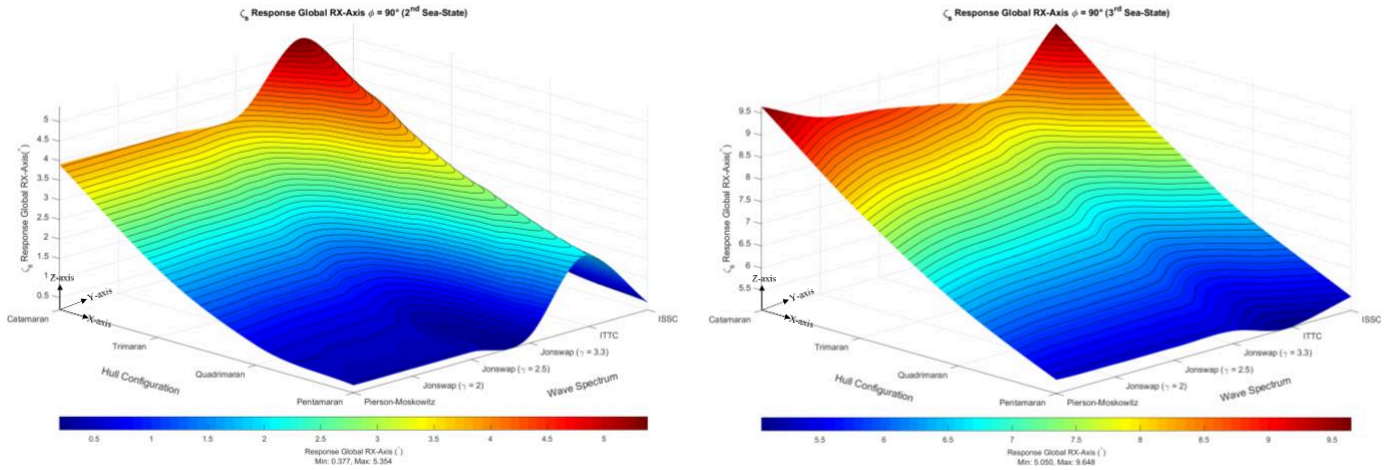
Figure 19 (a) shows that in sea-state 2, the conservative value is found in the catamaran configuration with the ITTC spectrum at approximately 3.80°, while the minimum value is in the pentamaran configuration with the JONSWAP $\gamma = 3.3$ spectrum at around 0.63°.

Figure 19 (b) highlights a marked contrast in the FPV response for sea-state 3. The catamaran configuration records the highest value of 6.84° under the Pierson-Moskowitz (PM) or ISSC wave spectrum. In contrast, the pentamaran configuration shows the lowest value of 4.33°, observed under the ITTC spectrum.

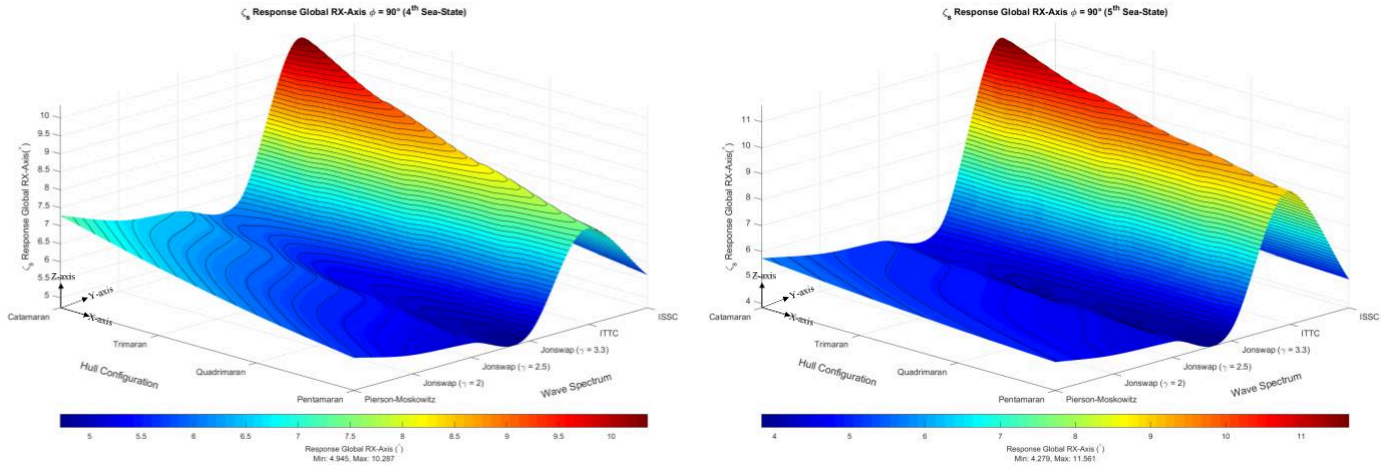
In **Figure 19 (c)**, sea-state 4 shows the peak value in the ITTC wave spectrum is 7.28°, while the JONSWAP spectrum with $\gamma = 3.3$ has a minimum value of 3.79°. This is notable because the quantitative value distinction is 1.92 times higher.

Finally, **Figure 19 (d)** for sea-state 5 indicates a similar trend to the previous conditions, but the maximum significant motion amplitude is around 8.18°, and the minimum is about 3.17°, showing a difference of approximately 2.58 times higher.

5.3.4. ζ_s Response Global RX-Axis (θ) with φ = 90°



(a) (b)



(c) (d)

712 **Figure 20**. ζ_s of roll in wave heading 90° : (a) H_s = 0.50 m, (b) H_s = 1.25 m, (c) H_s = 2.50 m, (d) H_s = 4.00 m

713

714 **Figure 20** presents a general trend consistent with the previous matter (φ = 45°), but with higher amplitude
715 responses due to the dominance of roll motion in the wave heading, φ = 90°.

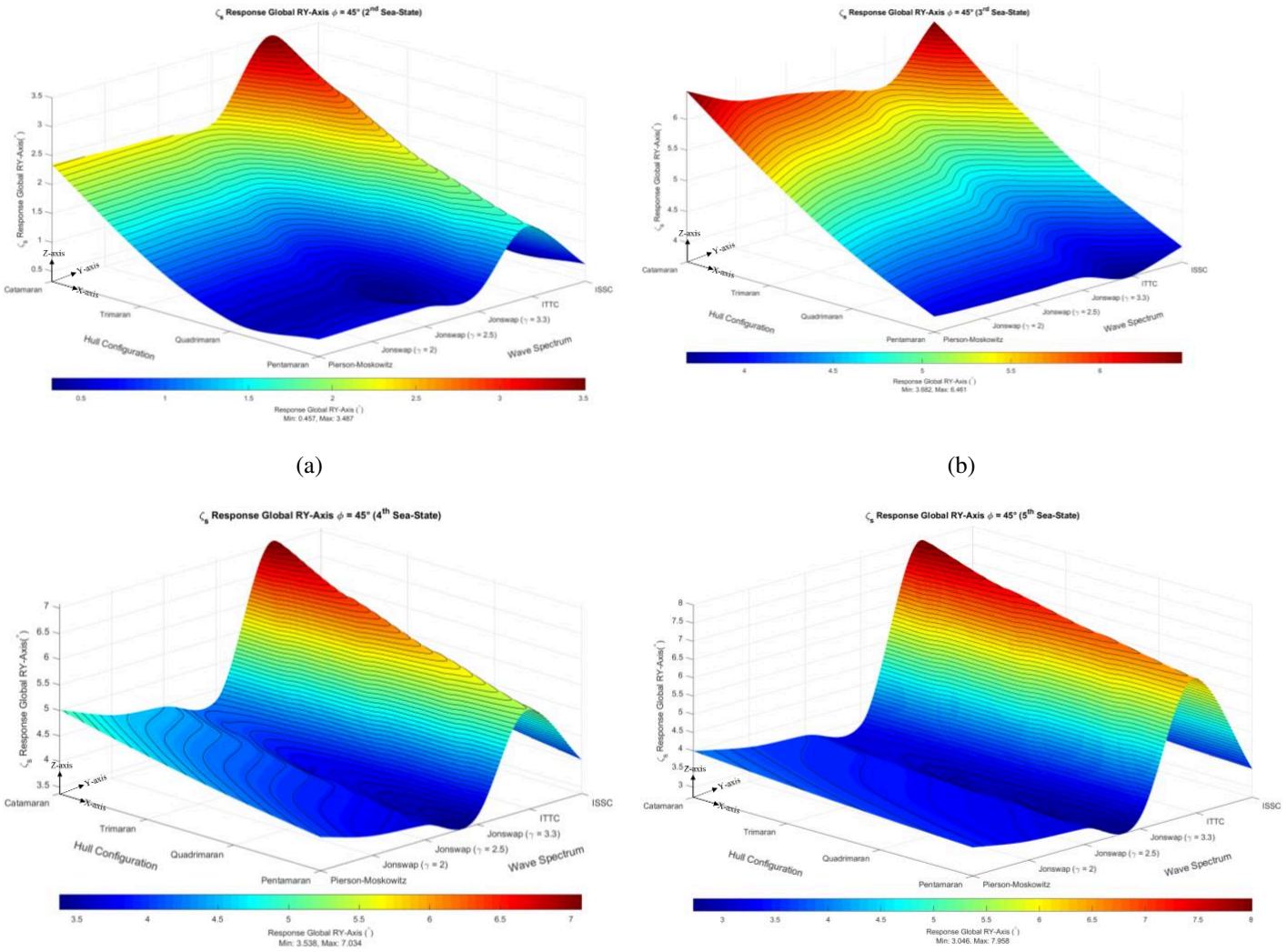
716 In **Figure 20 (a)**, for sea-state 2, the ITTC wave spectrum shows the most conservative trend with a response
717 amplitude of 5.35°, whereas the JONSWAP spectrum with γ = 3.3 presents a minimum value of approximately
718 0.38°.

719 A notable contrast is observed in **Figure 20 (b)**, which represents sea-state 3. In this case, the most conservative
720 value is found in the PM or ISSC wave spectrum for the catamaran configuration, with an amplitude of 9.65°,
721 while the minimum response is recorded at 5.05° for the pentamaran configuration under the ITTC spectrum.

722 In **Figure 20 (c)**, sea-state 4 shows the peak value in the ITTC wave spectrum as 10.29°, while the JONSWAP
723 spectrum with γ = 3.3 has a minimum value of 4.95°. This is notable because the quantitative value distinction is
724 2 times higher.

725 Finally, **Figure 20 (d)** depicts sea-state 5, where the trend is similar to previous conditions, but with a significant
726 difference in maximum amplitude. The peak response reaches 11.56°, while the minimum value is around 4.28°,
727 representing a notable difference of about 2.70 times higher.

5.3.5. ζ_s Response Global RY-Axis (ϕ) with $\varphi = 45°$



(a) (b)

(c) (d)

Figure 21. ζ_s of pitch in wave heading 45° : (a) H_s = 0.50 m, (b) H_s = 1.25 m, (c) H_s = 2.50 m, (d) H_s = 4.00 m

Figure 21 provides an overview of the pitch motion trends, which generally have a similar pattern to those observed in roll motion in all proposed models and wave spectrums. This section specifically focuses on a wave heading, $\varphi = 45°$, as the RAO values across all models exhibit similar behaviour in regular waves within wave heading, $\varphi = 0°$.

In **Figure 21 (a)**, sea-state 2 reveals the most conservative trend in the ITTC wave spectrum, with an amplitude of 3.49°. In contrast, the JONSWAP spectrum with $\gamma = 3.3$ shows a minimum value of approximately 0.46°.

Figure 21 (b) highlights a significant difference for sea-state 3, where the most conservative value is observed in the PM or ISSC wave spectrum for the catamaran configuration, with an amplitude pitch motion is 6.46°. Then for the minimum value is recorded at 3.68° for the pentamaran configuration under the ITTC spectrum.

In **Figure 21 (c)**, sea-state 4 is illustrated. The peak value in the ITTC wave spectrum is 7.03°, whereas the JONSWAP spectrum with $\gamma = 3.3$ exhibits a minimum value of 3.54°. This significant difference is noteworthy, as the peak value is more than 1.98 times higher than the minimum one.

Lastly, **Figure 21 (d)** illustrates sea-state 5, where the trend remains similar to previous sea-state conditions but with a significant difference in maximum amplitude. The peak response reaches 7.96°, while the minimum value is around 3.05°, indicating a notable difference of about 2.60 times higher than the minimum one.

6. Conclusions

An investigation was conducted to explore the influence of platform configuration, environmental conditions, and the sensitivity of different types of wave spectra on the performance of FPV structures. Numerical simulations using BEM techniques, based on the 3-D panel diffraction method, were employed to analyze the pure oscillatory motions in heave, pitch, and roll for all proposed designs. The results show that the FPV structure with five floating hulls (pentamaran) exhibits the lowest pure oscillatory motion response compared to other configurations under all sea state scenarios and different types of wave spectra. Numerical results show that the FPV structure with a five-hull configuration has the lowest motion response during pure oscillatory motion when compared to other configurations across various sea state scenarios. Additionally, there is a negative linear trend in the motion response of the FPV structure from catamaran to pentamaran configurations. This trend is due to the lateral addition of hulls, which increases the metacentric height and significantly reduces the excitation forces caused by roll motion. This reduction is associated with the natural period of motion, lateral acceleration, and enhanced transverse stability, ultimately improving the structure's stability during rolling motion at each respective type of proposed wave spectrum. Generally, the ITTC wave spectrum provides more conservative results compared to the PM, JONSWAP, and ISSC spectrums. This conservative trend is particularly evident in heave motion under sea-state conditions 2 and 3, and in roll and pitch motions under sea-state conditions 2, 4, and 5. This is influenced by the quantity of the area under the wave energy spectrum curve, which is associated with the RAO curve to form the FPV structure's response energy curve. The PM, JONSWAP, and ISSC spectra have relatively narrower shapes with higher peaks, compared to the wider ITTC curve. Therefore, the wave energy in the ITTC spectrum is capable of generating a more conservative excitation motion. Future research should focus on selecting mooring configurations and optimizing floater design for FPV technology. Optimization efforts can involve geometry modifications that reference various forms of offshore floating structures such as semi-submersible, SPAR, and others. It aims to advance sustainable development by optimizing the floater geometry to achieve optimal motion

compatibility compared to previous designs. In addition, the investigation of the hydrodynamic response of the mooring lines and FPV structure through time domain analysis is also recommended.

7. Acknowledgements

The authors express their gratitude to Institut Teknologi Sepuluh Nopember for providing research funding through the Outbound Researcher Mobility (ORM) program for the 2023/2024 period, batch 2 under contract number 2432/IT2/T/HK.00.01/2023.

8. CRediT authorship contribution statement

Mohammad Izzuddin Jifaturrohman: Methodology; software; validation; formal analysis; investigation; resources; writing – original draft; writing – review & editing; visualization. **I Ketut Aria Pria Utama**: Conceptual; investigation; writing – review & editing; supervision; project administration; funding acquisition. **Teguh Putranto**: Validation; investigation; writing – review & editing; supervision. **Dony Setyawan**: Investigation; writing – review & editing. **Luofeng Huang**: Investigation; writing – review & editing; supervision.

9. Declaration of Competing Interest

The authors declare that there are no financial conflicts of interest or personal relationships that could have influenced the work presented in this paper.

10. References

American Bureau of Shipping (ABS)., 2016. Guidance Notes on Selecting Design Wave by Long Term Stochastic Method. Houston, USA. www.eagle.org

Alves, M., 2016. Frequency-Domain Models in Numerical Modelling of Wave Energy Converters: State-of-the-Art Techniques for Single Devices and Arrays (pp. 11–30). Elsevier. https://doi.org/10.1016/B978-0-12-803210-7.00002-5

Ansys., 2012. Ansys Aqwa Theory Manual. Canonsburg, USA.

Ballard, E.J., 2002. Time Domain Simulation of Ship Motions in Waves. PhD Thesis, University of Southampton, Faculty of Engineering and Applied Science, School of Engineering Sciences, Ship Science.

Bertram, V., 2012. Ship Seakeeping. In Practical Ship Hydrodynamics (pp. 143–204). Elsevier. https://doi.org/10.1016/b978-0-08-097150-6.10004-1

800 Bhattacharyya, R., 1978. Dynamics of Marine Vehicles. John Wiley & Sons, USA.
801 Bosma Br., Zhang Zhe., Brekken Ted K.A., Ozkan H. Tuba., Mc Natt Cameron., C Yim Solomon., 2012. Wave
802 Energy Converter Modeling in the Frequency Domain: A Design Guide. IEEE, 2099–2106.
803 https://doi.org/10.1109/ECCE.2012.6342553
804 Bošnjaković, M., Santa, R., Crnac, Z., & Bošnjaković, T., 2023. Environmental Impact of PV Power Systems.
805 Sustainability (Switzerland), 15(15). https://doi.org/10.3390/su151511888
806 Bretschneider, C. L., 1952. The Generation and Decay of Wind Waves in Deep Water, In: American Geophysical
807 Union (Vol. 33, Issue 3). https://doi.org/10.1029/TR033i003p00381
808 Bretschneider, C. L., 1963. A One-Dimensional Gravity Wave Spectrum. Ocean Wave Spectra, pp 41–56.
809 Bunnik, T.H.J., Huijsmans, R.H.M., Kapsenberg, G.K., et al., 2010. A comparative study on the state-of-the-art
810 prediction tools for seakeeping. In: Proceedings of the 28th Symposium on Naval Hydrodynamics,
811 Pasadena, California, USA, 12–17 September 2010. Delft University of Technology, Report No. 1699-P.
812 Cao, Y., Cao, D., He, G., Ge, X., Hao, Y., 2021. Modelling and vibration analysis for the multi-plate structure
813 connected by nonlinear hinges. Journal of Sound and Vibration. 492, 115809.
814 https://doi.org/10.1016/j.jsv.2020.115809
815 Cazzaniga, R., Cicu, M., Rosa-Clot, M., Rosa-Clot, P., Tina, G. M., Ventura, C., 2018. Floating photovoltaic
816 plants: Performance analysis and design solutions, in: Renewable and Sustainable Energy Reviews. 81,
817 Elsevier Ltd., pp. 1730–1741. https://doi.org/10.1016/j.rser.2017.05.269
818 Cazzaniga, R., Rosa-Clot, M., 2021. The booming of floating PV. Solar Energi. 219, 3–10.
819 https://doi.org/10.1016/j.solener.2020.09.057
820 Chakrabarti, S. K., 2005. Handbook of Offshore Engineering. Elsevier. Plainfield, USA.
821 https://shop.elsevier.com/books/handbook-of-offshore-engineering-volume-1/chakrabarti/978-0-08-
822 044568-7
823 Chen, M., Guo, H., Wang, R., Tao, R., Cheng, N., 2021. Effects of gap resonance on the hydrodynamics and
824 dynamics of a multi-module floating system with narrow gaps. Journal of Marine Science and Engineering,
825 9(11). https://doi.org/10.3390/jmse9111256
826 Chen, X., Liang, H., 2016. Wavy properties and analytical modeling of free-surface flows in the development of
827 the multi-domain method. Journal of Hydrodynamics, 28(6), 971–976. https://doi.org/10.1016/S1001-
828 6058(16)60698-4

Choi, Y., Lee, J., 2015. Structural Safety Assessment of Ocean-Floating Photovoltaic Structure Model. Israel Journal of Chemistry. 55(10), 1081–1090. https://doi.org/10.1002/ijch.201400197

Claus, R., López, M., 2022. Key issues in the design of floating photovoltaic structures for the marine environment. Renewable and Sustainable Energy Reviews. 164, 112502. https://doi.org/10.1016/j.rser.2022.112502

CSI Solar Co. Ltd., 2021. Preliminary Technical Information Sheet of Canadian Solar. Cremorne, Australia. https://static.csisolar.com/wp-content/uploads/sites/2/2020/06/02103821/Canadian_Solar-Datasheet-CS6W-MB-AG-520-550-V1.0C3_AU.pdf (accessed 30 July 2024).

Friel, D., Karimirad, M., Whittaker, T., Doran. J., 2020. Developments in Renewable Energies Offshore, in: C. Guedes Soares. (1st Edition). CRC Press. https://doi.org/10.1201/9781003134572

Delacroix, S., Bourdier, S., Soulard, T., Elzaabalawy, H., Vasilenko, P., 2023. Experimental Modelling of a Floating Solar Power Plant Array under Wave Forcing. Energies. 16(13). https://doi.org/10.3390/en16135198

Det Norske Veritas., 2010. Recommended Practice Environmental Conditions and Environmental Loads. http://www.dnv.com

Djatmiko, E. B., 2012. The Behavior and Operability of Offshore Structure in Random Waves. ITS Press, Indonesia. https://www.researchgate.net/publication/335620271_Perilaku_dan_Operabilitas_Bangunan_Laut_di_Atas_Gelombang_Acak (accessed 20 July 2024)

Essak, L., Ghosh, A., 2022. Floating Photovoltaics: A Review. Clean Technologies. 4(3), 752–769. https://doi.org/10.3390/cleantechnol4030046

Faltinsen, O.M., 1990. Sea Loads on Ships and Offshore Structures. Cambridge University Press.

Ghosh, A., 2023. A comprehensive review of water based PV: Flotavoltaics, under water, offshore & canal top, in: Ocean Engineering. 281, Elsevier Ltd. https://doi.org/10.1016/j.oceaneng.2023.115044

Guha, A., 2016. Development and Application of A Potential Flow Computer Program: Determining First and Second Order Wave Forces at Zero and Forward Speed in Deep and Intermediate Water Depth. https://hdl.handle.net/1969.1/156999 (accessed 20 July 2024).

Haug, Ø., Trym, L., Sjøberg, S., 2018. Evaluation and Comparison of Operability and Operational Limits of Service Vessel Designs in Exposed Aquaculture. http://hdl.handle.net/11250/2567227 (accessed 20 July 2024).

He, G. H., 2014. An iterative Rankine boundary element method for wave diffraction of a ship with forward speed. Journal of Hydrodynamics, 26(5), 818–826. https://doi.org/10.1016/S1001-6058(14)60090-1

He, G., & Kashiwagi, M., 2014. A time-domain higher-order boundary element method for 3D forward-speed radiation and diffraction problems. Journal of Marine Science and Technology (Japan), 19(2), 228–244. https://doi.org/10.1007/s00773-013-0242-1

Hu, C., Sueyoshi, M., Liu, C., Kyozuka, Y., Ohya, Y., 2013. Numerical and Experimental Study on a Floating Platform for Offshore Renewable Energy. in: Ocean Renewable Energi. (Volume 8). https://doi.org/10.1115/OMAE2013-11133

Huston, S., 2010. Structural Health Monitoring of a High Speed Naval Vessel Using Ambient Vibrations. https://www.researchgate.net/publication/44226379

IEA., 2022. CO2 Emissions in 2022. www.iea.org (accessed 04 August 2024).

IEA., 2023. Snapshot of Global PV Markets 2023: Task 1 Strategic PV Analysis and Outreach PVPS. M. Gaëtan, Ed., International Energy Agency. www.iea-pvps.org (accessed 04 August 2024).

ITTC., 1975. 14th International Towing Tank Conference. International Towing Tank Conference. https://repository.tudelft.nl/record/uuid:9d57e745-61cc-4e9c-9f0d-c98c659059b2 (accessed 04 August 2024).

ITTC. (2012). 27th International Towing Tank Conference. International Towing Tank Conference. https://ittc.info/downloads/proceedings/27th-conference-copenhagen-2014/

ITTC., 2023. 23rd International Towing Tank Conference. The Specialist Committee on Waves. https://www.ittc.info/media/1469/waves.pdf (accessed 04 August 2024).

J. Pierson, W., Moskowitz, L., 1963. A proposed spectral form for fully developed wind seas based on the similarity theory of S. A. Kitaigorodskii. https://doi.org/10.1029/JZ069i024p05181

Jifaturrohman, M. I., Putranto, T., Utama, I. K. A. P., Huang, L., 2024. Effect of Platform Configurations and Environmental Conditions on the Performance of Floating Solar Photovoltaic Structures. International Marine Design Conference (IMDC). https://doi.org/10.59490/imdc.2024.854

K. Hasselmann., T.P. Barnett., E. Bouws., H. Carlson., D.E. Cartwright., K. Enke., J.A. Ewing., H. Gienapp., D.E Hasselmann., P. Kruseman., A. Meerburg., P. Muller., D.J. Olbers., K. Ritcher., W. Sell., H. Walden., 1973. Measurements of Wind-Wave Growth and Swell Decay during the Joint North Sea Wave Project (JONSWAP). https://repository.tudelft.nl/record/uuid:f204e188-13b9-49d8-a6dc-4fb7c20562fc (accessed 04 August 2024)

Kara, F., 2022. Time domain potential and source methods and their application to twin-hull high-speed crafts. Ships and Offshore Structures. https://doi.org/10.1080/17445302.2022.2035560

He, G., Kashiwagi, M., 2014. Radiation-problem solutions using a time-domain iterative HOBEM. International Journal of Offshore and Polar Engineering, 24(2), 81–89. http://www.isope.org/publications

Lagemann, B., 2019. Efficient seakeeping performance predictions with CFD. Degree Project, KTH Royal Institute of Technology, Stockholm, Sweden.

Lee, J. H., Paik, K. J., Lee, S. H., Hwangbo, J., Ha, T. H., 2022. Experimental and Numerical Study on the Characteristics of Motion and Load for a Floating Solar Power Farm under Regular Waves. Journal of Marine Science and Engineering. 10(5). https://doi.org/10.3390/jmse10050565

Lewandowski, E. M., 2008. Multi-vessel seakeeping computations with linear potential theory. Ocean Engineering, 35(11–12), 1121–1131. https://doi.org/10.1016/j.oceaneng.2008.04.011

Lewis V, E., 1988. Principles Of Naval Architecture (second revision, Vol. 1). SNAME. https://www.sname.org/principles-naval-architecture (accessed 04 August 2024)

Li, A., & Li, Y., 2019. Numerical and Experimental Study on Seakeeping Performance of a High-Speed Trimaran with T-foil in Head Waves. Polish Maritime Research, 26(3), 65–77. https://doi.org/10.2478/pomr-2019-0047

Li, Z., Chen, D., Feng, X., 2023. Hydroelastic and expansibility analysis of a modular floating photovoltaic system with multi-directional hinge connections. Ocean Engineering. 289. https://doi.org/10.1016/j.oceaneng.2023.116218

Liang, H., & Chen, X., 2017. A new multi-domain method based on an analytical control surface for linear and second-order mean drift wave loads on floating bodies. Journal of Computational Physics, 347, 506–532. https://doi.org/10.1016/j.jcp.2017.07.014

Liu, H., Krishna, V., Lun Leung, J., Reindl, T., Zhao, L., 2018. Field experience and performance analysis of floating PV technologies in the tropics. Progress in Photovoltaics: Research and Applications. 26(12), 957–967. https://doi.org/10.1002/pip.3039

Michailides, C., Loukogeorgaki, E., Angelides, D. C., 2013. Response analysis and optimum configuration of a modular floating structure with flexible connectors. Applied Ocean Research. 43, 112–130. https://doi.org/10.1016/j.apor.2013.07.007

Murdijanto, Utama, I. K. A. P., Jamaluddin, A., 2011. An Investigation Into the Resistance/Powering and Seakeeping Characteristics of River Catamaran and Trimaran. Makara of Technology Series. 15(1). https://doi.org/10.7454/mst.v15i1.853

Newman, J.N., 1977. Marine Hydrodynamics. MIT Press, Cambridge, Massachusetts, London, England.

Newman, J.N., 1979. The theory of ship motions. Advances in Applied Mechanics, 18, 221–283. https://doi.org/10.1016/S0065-2156(08)70268-0

Oliveira-Pinto, S., Stokkermans, J., 2020. Assessment of the potential of different floating solar technologies – Overview and analysis of different case studies. Energy Conversion and Management. 211, 112747. https://doi.org/10.1016/j.enconman.2020.112747

Orcina Ltd. (2024). General data: Dynamics for Solution method. https://www.orcina.com/webhelp/OrcaFlex/Content/html/Generaldata,Dynamics.htm

Pacuraru, F., Domnisoru, L., & Pacuraru, S., 2020. On the comparative seakeeping analysis of the full scale kcs by several hydrodynamic approaches. Journal of Marine Science and Engineering, 8(12), 1–32. https://doi.org/10.3390/jmse8120962

Pimentel Da Silva, G. D., Branco, D. A. C., 2018. Is floating photovoltaic better than conventional photovoltaic? Assessing environmental impacts. Impact Assessment and Project Appraisal. 36(5), 390–400. https://doi.org/10.1080/14615517.2018.1477498

Pouran, H. M., Padilha, M., Lopes, C., Nogueira, T., Alves, D., Branco, C., Sheng, Y., 2022. Environmental and technical impacts of floating photovoltaic plants as an emerging clean energy technology. IScience Perspective. 25, 1–16. https://doi.org/10.1016/j.isci

Sclavounos, P.D., Nakos, D.E., 1990. On steady and unsteady ship wave patterns. Journal of Fluid Mechanics, 215, 263–288. https://doi.org/10.1017/S0022112090002646.

Shao, Y. L., & Faltinsen, O. M., 2014. A numerical study of the second-order wave excitation of ship springing by a higher-order boundary element method. International Journal of Naval Architecture and Ocean Engineering, 6(4), 1000–1013. https://doi.org/10.2478/IJNAOE-2013-0227

Song, J., Kim, J., Lee, J., Kim, S., Chung, W., 2022. Dynamic Response of Multiconnected Floating Solar Panel Systems with Vertical Cylinders. Journal of Marine Science and Engineering. 10(2). https://doi.org/10.3390/jmse10020189

945 Suastika, K., Silaen, A., Aliffrananda, M. H. N., Hermawan, Y. A., 2021. Seakeeping analysis of a hydrofoil
946 supported watercraft (Hysuwac): A case study. CFD Letters. 13(5), 10–27.
947 https://doi.org/10.37934/cfdl.13.5.1027
948 Tajali, Z., & Shafieefar, M., 2011. Hydrodynamic analysis of multi-body floating piers under wave action. Ocean
949 Engineering, 38(17–18), 1925–1933. https://doi.org/10.1016/j.oceaneng.2011.09.025
950 Tang, H., Zhang, X., Ren, H., & Yu, P., 2020. Numerical study of trimaran motion and wave load prediction
951 based on time-domain Rankine-Green matching method. Ocean Engineering, 214.
952 https://doi.org/10.1016/j.oceaneng.2020.107605
953 Tang, K., Zhen, Q. Z., Hong, L., Jiang, D. P., Chen, X., & Li, Y. L., 2021. Time-domain analysis of side-by-side
954 floating bodies by the three-dimensional hybrid Green function method. Ships and Offshore Structures,
955 16(5), 516–528. https://doi.org/10.1080/17445302.2020.1742493
956 Ten I., Chen X. B. A coupled Rankine-Green function method applied to the forward-speed seakeeping problem
957 [C]. Proceedings 25th International Workshop on Water Waves and Floating Bodies. Harbin, China, 2010,
958 165–168
959 Trapani, K., Millar, D. L., 2016. Hydrodynamic Overview Of Flexible Floating Thin Film PV Arrays. Proceeding
960 of the 3rd Offshore Energy and Storage Symposium. 13–15.
961 https://www.researchgate.net/publication/308900964
962 Vyas, M., Chowdhury, S., Verma, A., Jain, V. K., 2022. Solar Photovoltaic Tree: Urban PV power plants to
963 increase power to land occupancy ratio. Renewable Energi. 190, 283–293.
964 https://doi.org/10.1016/j.renene.2022.03.129
965 Wackers, J., Koren, B., Raven, H. C., van der Ploeg, A., Starke, A. R., Deng, G. B., Queutey, P., Visonneau, M.,
966 Hino, T., & Ohashi, K., 2011. Free-Surface Viscous Flow Solution Methods for Ship Hydrodynamics.
967 Archives of Computational Methods in Engineering, 18(1), 1–41. https://doi.org/10.1007/s11831-011-
968 9059-4
969 Wang, J., Lund, P. D., 2022. Review of Recent Offshore Photovoltaics Development, in: Energies. 15(20), MDPI.
970 https://doi.org/10.3390/en15207462
971 Wang, Z., Carriveau, R., Ting, D. S. K., Xiong, W., Wang, Z., 2019. A review of marine renewable energy storage,
972 in: International Journal of Energy Research. 43(12). John Wiley and Sons Ltd., pp. 6108–6150.
973 https://doi.org/10.1002/er.4444

Wehausen, J. V., & Laitone, E. V., 1960. Surface Waves (pp. 446–778). Springer, Berlin, Heidelberg. https://doi.org/10.1007/978-3-642-45944-3_6

Wei, Y., Ou, B., Wang, J., Yang, L., Luo, Z., Jain, S., Hetharia, W., Riyadi, S., Utama, I., Huang, L., 2023. Simulation of a floating solar farm in waves with a novel sun-tracking system. IOP Conference Series: Materials Science and Engineering. 1288(1), 012041. https://doi.org/10.1088/1757-899x/1288/1/012041

Wei, Y., Zou, D., Zhang, D., Zhang, C., Ou, B., Riyadi, S., Utama, I. K. A. P., Hetharia, W., Wood, T., Huang, L., 2024. Motion characteristics of a modularized floating solar farm in waves. Physics of Fluids. 36(3). https://doi.org/10.1063/5.0199248

World Bank Group, E. and S., 2019. Where Sun Meets Water: Floating Solar Handbook for Practitioners. World Bank. www.worldbank.org (accessed 04 August 2024)

Xie, M., Jia, T., Dai, Y., 2022. Hybrid photovoltaic/solar chimney power plant combined with agriculture: The transformation of a decommissioned coal-fired power plant. Renewable Energi. 191, 1–16. https://doi.org/10.1016/j.renene.2022.03.148

Xu, C., Ren, H., Zhou, X., Sutulo, S., Guedes Soares, C., & Li, C., 2020. Analysis of Numerical Errors of the Hess Smith Panel Method With Asymmetric Meshes. Journal of Offshore Mechanics and Arctic Engineering, 142(2). https://doi.org/10.1115/1.4045189

Xu, P., & Wellens, P. R., 2022a. Theoretical analysis of nonlinear fluid–structure interaction between large-scale polymer offshore floating photovoltaics and waves. Ocean Engineering. 249, 110829. https://doi.org/10.1016/j.oceaneng.2022.110829

Xu, P., Wellens, P. R., 2022b. Fully nonlinear hydroelastic modeling and analytic solution of large-scale floating photovoltaics in waves. Journal of Fluids and Structures. 109, 103446. https://doi.org/10.1016/j.jfluidstructs.2021.103446

Yan, C., Shi, W., Han, X., Li, X., Verma, A. S., 2023. Assessing the dynamic behavior of multiconnected offshore floating photovoltaic systems under combined wave-wind loads: A comprehensive numerical analysis. Sustainable Horizons. 8. https://doi.org/10.1016/j.horiz.2023.100072

Yan, H., Chong, D., Wang, Z., Liu, M., Zhao, Y., Yan, J., 2022. Dynamic performance enhancement of solar-aided coal-fired power plant by control strategy optimization with solar/coal-to-power conversion characteristics. Energi. 244. https://doi.org/10.1016/j.energy.2021.122564

Zhang, C., Dai, J., Ang, K. K., Lim, H. V., 2024. Development of compliant modular floating photovoltaic farm for coastal conditions. Renewable and Sustainable Energy Reviews. 190. https://doi.org/10.1016/j.rser.2023.114084

Zhang, D., Yuan, Z. M., Du, J., Li, H., 2022. Hydrodynamic modelling of large arrays of modularized floating structures with independent oscillations. Applied Ocean Research. 129. https://doi.org/10.1016/j.apor.2022.103371

Zhang, D., Du, J., Yuan, Z., Yu, S., Li, H., 2023. Motion characteristics of large arrays of modularized floating bodies with hinge connections. Physics of Fluids. 35(7). https://doi.org/10.1063/5.0153317

Zhao, B., Jiang, H., Sun, J., Zhang, D., 2023. Research on the Hydrodynamic Performance of a Pentamaran in Calm Water and Regular Waves. Applied Sciences (Switzerland). 13(7). https://doi.org/10.3390/app13074461

Zheng, X., Zheng, H., Lei, Y., Li, Y., Li, W., 2020. An Offshore Floating Wind–Solar–Aquaculture System: Concept Design and Extreme Response in Survival Conditions. Energies. 13(3), 604. https://doi.org/10.3390/en13030604



https://dspace.org/

A study into the correlation between single array-hull configurations and wave spectrum for floating solar photovoltaic systems

Jifaturrohman, Mohammad Izzuddin; Utama, I Ketut Aria Pria; Putranto, Teguh; Setyawan, Dony; Huang, Luofeng

2024-11-15
Elsevier
https://doi.org/10.1016/j.oceaneng.2024.119312
Jifaturrohman MI, Utama IKAP, Putranto T, et al., (2024) A study into the correlation between single array-hull configurations and wave spectrum for floating solar photovoltaic systems. Ocean Engineering, Volume 312, November 2024, Article number 119312

Downloaded from a DSpace repository. https://dspace.org/